# FOCUS REVIEWS

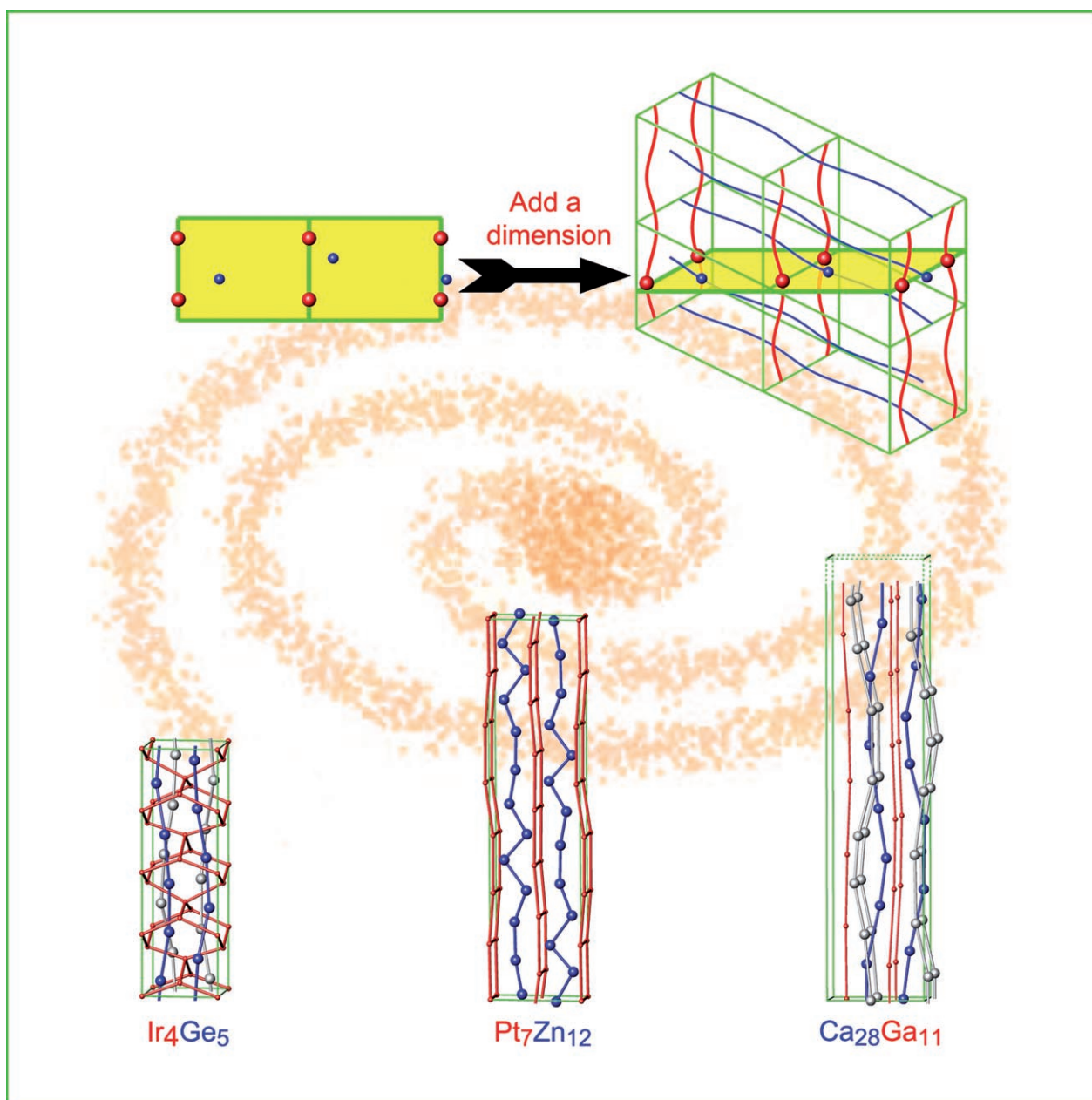# Four-Dimensional Space Groups for Pedestrians: Composite Structures

Junliang Sun,*[a] Stephen Lee,*[a] and Jianhua Lin*[b]

*Dedicated to Professor Roald Hoffmann on the occasion of his retirement*

**Abstract:** Higher-dimensional crystals have been studied for the last thirty years. However, most practicing chemists, materials scientists, and crystallographers continue to eschew the use of higher-dimensional crystallography in their work. Yet it has become increasingly clear in recent years that the number of higher-dimensional systems continues to grow from hundreds to as many as a thousand different compounds. Part of the problem has to do with the somewhat opaque language that has developed over the past decades to describe higher-dimensional systems. This language, while well-suited to the specialist, is too sophisticated for the neophyte wishing to enter the field, and as such can be an impediment. This Focus Review hopes to address this issue. The goal of this article is to show the regular chemist or materials scientist that knowledge of regular 3D crystallography is all that is really necessary to understand 4D crystal systems. To this end, we have couched higher-dimensional composite structures in the language of ordinary 3D crystals. In particular, we developed the principle of complementarity, which allows one to identify correctly 4D space groups solely from examination of the two 3D components that make up a typical 4D composite structure.

**Keywords:** composite compounds · host–guest systems · incommensurate structures · intermetallic phases · super-space group

## 1. Introduction

The pedestrian we refer to in the title is a regular materials chemist, solid-state chemist, or crystallographer, someone with a firm background in regular crystals, someone who, like us, has his or her understanding of crystal space groups firmly embedded in the 230 space groups of Volume A of the International Tables.[1] This article is especially for the regular crystallographer who, like us, has become both intrigued and befuddled by the large number of recent articles that speak of four-, five-, and even six-dimensional crystals,[2–6]1 articles that talk about space groups such as $I4_1/amd(00\gamma)00ss$[7–10] and $R\bar{3}m(00\gamma)0s$,[11,12] space-group names whose meaning we, as ordinary crystallographers, can only guess.

The goal of this review is twofold. The first goal is to introduce a methodology for the determination of the space group for one class of higher-dimensional structures: composite systems.[6–8,13,14] The methodology is based on the idea that for higher-dimensional crystals, just as in ordinary 3D crystals, the easiest way to determine a space group is by careful examination of the real crystal structure. In this, we differ significantly from many of the previous literature accounts of higher-dimensional crystallography.[7,15–21]2 Previous literature accounts of composite structures, for example, that given in Volume C of the International Tables,[23] always rely in part, and sometimes wholly, on a reciprocal-space approach for the identification of higher-dimensional space-group symmetry. By contrast, the concept of reciprocal space will not be used at all herein.3

[a] Dr. J. Sun, Prof. S. Lee
Department of Chemistry and Chemical Biology
Baker Laboratory, Cornell University
Ithaca, NY 14853-1301 (USA)
Fax: (+1) 607-255-4137
E-mail: junliang.sun@gmail.com
          sl137@cornell.edu

[b] Prof. J. Lin
College of Chemistry and Molecular Engineering
Peking University, Beijing 100871 (China)
Fax: (+86) 10-627-53-541
E-mail: jhlin@pku.edu.cn

Supporting information for this article is available on the WWW under http://www.chemasianj.org or from the author.

---

1 Higher-dimensional crystals: The International Tables for Crystallography Volume C refers to higher-dimensional crystals as incommensurate crystals. Herein, we refer to these same systems as higher-dimensional crystals to emphasize the essential point that incommensurate crystals are only crystals, that is, they have translational symmetry, when more than three (higher) dimensions are used.

2 By contrast, a real-space account of modulated structures has been previously given.[22]

3 The focus of this article is the determination of the higher-dimensional space group once a 3D crystal structure has been determined (this step can be, and often is, achieved through the determination of a 3D commensurate crystal structure). We therefore assume herein that we are dealing with a specific chemical system for which the 3D diffraction problem has been solved. The chemical systems considered in this article are based on those crystal structures reported in the last full compendium of intermetallic crystal structures known to us: Pearson's Handbook of Crytallographic Data for Intermetallic Phases.[24] We made one exception to this self-imposed limitation: we included all known higher-dimensional composite elemental structures.

The methods in this Focus Review are applied to composite structures. A composite structure is a system that readily decomposes into two separate subunits, each with their own separate lattice constants. (We will give specific examples of such compounds in this article: elemental structures under high pressure, Rb-IV[25,26] and Sc-II,[27,28] binary systems such as $Ir_3Ga_5$[29] and $Pt_7Zn_{12}$,[30] and more complex formulations such as $Ba_9Fe_{16}S_{32}$.[31–33]) However, by being introduced to this single class of higher-dimensional crystals, the reader would hopefully become more at ease with other classes of higher-dimensional crystals, quasicrystals,[34–39] and modulated structures.[40–51]

We show herein that for composite crystals the determination of higher-dimensional space groups is quick, if one just looks at the crystal structure itself. By that we do not mean looking at a 4D crystal structure (which sounds to us a daunting task), but rather looking at the composite 3D systems that form the physical basis of the higher-dimensional crystal. In this way, we found that the only change from ordinary crystallography is that one has to examine at least two 3D crystals (one for each component of the composite) to derive a correct space-group name.

At the same time, there is another goal underlying this account. We wish to show that the newfangled nomenclature of crystallographic space groups is very manageable, especially if one already understands the names of the original 230 space groups. For those readers patient enough to work through this article, we hope that by its conclusion, they would not only understand the symbols of the higher-dimensional space groups, but also be able to name the higher-dimensional space groups correctly when describing new and interesting crystalline systems.

In doing so, we wish to show that it is actually worthwhile to use the new higher-dimensional nomenclature, as the new names actually simplify our understanding of a good number of the more complex structures with which we routinely deal. As our own expertise tends toward the intermetallic side of materials chemistry, the examples we chose come from this branch of materials chemistry. We consider for much of this article the Nowotny chimney–ladder phases,[7–9,29,52–56] a significant family of binary transition-metal and main-group-element compounds.

## 2. Prevalence of Higher-Dimensional Crystals

The motivation for understanding higher-dimensional crystallography is straightforward. We know now that higher-dimensional crystals are fairly common. They are found in compounds of almost all the elements in the periodic table and in crystals of every Bravais class.[6,8,39,41,58–62] At the same time, a description of such systems as higher-dimensional crystals leads to a true decrease in complexity: structures that contain hundreds (or even thousands) of atoms in the three-dimensional unit cell or even structures that are not crystalline at all in three dimensions reduce in higher dimensions to structures with just a handful of (typically one to five) atoms in the unit cell.

In this section we focus on data that illustrate the widespread nature of higher-dimensional crystals. We consider here intermetallic compounds (inorganic compounds that do not contain a halogen, noble gas, or oxygen atom in the chemical formula). By this definition (a standard one[24]), intermetallic compounds involve compounds of 80 of the first 92 elements in the periodic table.[4]

When we think of the crystal structures of such intermetallic compounds, we tend to think of simple crystal structures: the face-centered cubic close packing or the diamond structure. But an examination of the intermetallic structural database[24] shows that there are 1100 intermetallic compounds found in 260 structure types with over 100 atoms in

*Junliang Sun was born in 1979 in Suzhou, China and received his BSc (2001) and PhD (2006) in chemistry at Peking University (Prof. Jianhua Lin). He also worked at Cornell University as an exchange student and postdoctorate in 2004 and 2006 (Prof. Stephen Lee). He is currently a postdoctorate in Prof. Xiaodong Zou's group in Stockholm University. His research interests include structure determination with X-ray and electron-microscopy techniques and the physical properties of oxides and intermetallic compounds.*

*Stephen Lee has been a Professor in the Chemistry and Chemical Biology Department of Cornell University since 1998. His abiding interest in intermetallic crystals dates back to his training with Jeremy Burdett, Jean Rouxel, and Wolfgang Jeitschko.*

*Jianhua Lin was born in 1955 in Inner Mongolia, China. After receiving his PhD in chemistry at Peking Univ. in 1986 with Prof. Mianzeng Su and working as a postdoctoral fellow (1988–1991) with Prof. von Schneiring at the Max Plank Institute for Solid Research in Stuttgart and Prof. Gordon Miller at Iowa State Univ. (1991–1993), he was appointed Assoc. Prof. (1993) and became Full Prof. (1995) at Peking Univ. His research interests lie in the synthesis, structures, and physical properties of new solid-state compounds, including transition-metal oxides, borates, phosphates, and porous materials.*

---

4 We suspect that higher-dimensional compounds are just as frequently found in oxides and halides, but these latter compounds lie outside our expertise.

the unit cell. Such structures vary from compounds with simple stoichiometries such as $MgAu_3$[63] and $NaCd_2$[64] to more complex formulae such as $Ca_7Rh_{20}B_{14}$[65] and $Mg_{54}Ag_{17}$.[66] They are found in all seven of the crystal systems. Most if not all of these structures can be thought of as being quite involved and, to many of us, including the authors, mysterious.

Tables 1 and 2 list the primitive tetragonal and face-centered orthorhombic structures given in Pearson's Handbook[24] with over 100 atoms in the unit cell. Hydrides, borides, silicides, germanides, sulfides, nitrides, arsenides, and others are included in this list. Also included is a list of the subset of these complex structures that we can currently describe as higher-dimensional crystals. For these crystal classes, half of the large-unit-cell structures prove to be higher-dimensional crystals.

Table 1. Primitive tetragonal intermetallic structures with at least 100 atoms per unit cell.[a]

| Formula | Atoms | Type |
|---|---|---|
| $Nd_5Fe_{18}B_{18}$[b] | 328 | composite |
| $Mn_{27}Si_{47}$ | 296 | composite |
| $Sm_{17}Fe_{60}B_{60}$ | 274 | composite |
| $Gd_2Fe_7B_7$[b] | 256 | composite |
| $AlB_{12}$ | 216 | |
| $AlBeB_{22}$ | 212 | |
| $FeNb_2Si_2$ | 198 | |
| B | 196 | |
| $V_{17}Ge_{31}$ | 192 | composite |
| $Cd_3As_2$ | 160 | modulated |
| $Ho_6Mn_{23}H_{23}$ | 156 | |
| $Ta_4P_4S_{29}$ | 148 | composite |
| $Y_6Mn_{23}H_{23}$ | 148 | |
| $Mo_{13}Ge_{23}$ | 144 | composite |
| $Ba_5Fe_9S_{18}$ | 128 | composite |
| $TaTe_4$ | 160 | modulated |
| $Mn_{11}Si_{19}$ | 120 | composite |
| $Ba_9Fe_{16}S_{32}$ | 116 | composite |
| $Ce_2Fe_{14}BH_4$ | 112 | |
| $Rh_{10}Ga_{17}$ | 108 | composite |
| $Li_5Ce_{26}Ge_{22}$ | 108 | |

[a] Data source: Pearson's Handbook.[24] [b] These two structures may also be treated as orthorhombic.[57]

Table 2. Face-centered orthorhombic intermetallic structures with at least 100 atoms per unit cell.[a]

| Formula | Atoms | Type |
|---|---|---|
| $RbNa_6Ga_{20}$ | 928 | quasi. approx.[b] |
| $Na_5Li_3Ga_{20}$ | 920 | quasi. approx. |
| $EuGa_2S_4$ | 224 | modulated |
| $BaCdSnS_4$ | 224 | modulated |
| $Na_3LaN_6H_{12}$ | 176 | |
| $TlPbAs_3S_6$ | 176 | |
| $Ca_7Rh_{20}B_{14}$ | 164 | composite |
| $Cd_7P_{10}$ | 136 | |
| S | 128 | |
| $Sr_5Rh_{14}B_{10}$ | 116 | composite |
| $PrRh_5B_2$ | 116 | |
| $SrN_6$ | 112 | |

[a] Data source: Pearson's Handbook.[24] [b] quasi. approx. = quasicrystalline approximate.

In the Supporting Information we give similar tables for the remaining Bravais lattice types.[5] As these further tables show, roughly a third of all crystal structures with over 100 atoms in the unit cell can be described as higher-dimensional crystals.[6]

These tables further break down higher-dimensional crystals into three categories: composite structures, modulated structures, and quasicrystalline approximants.[38,39,58,67] Although the remainder of this article will investigate only one of these three categories, composite structures, it is hoped that a thorough understanding of this single class of higher-dimensional crystals would serve as an introduction to higher-dimensional crystallography in general.

## 3. Superstructures for Regular Crystallography

Before launching into our detailed description of how one can correctly obtain the name of a higher-dimensional space group, we begin by noting that the types of physical systems that can be treated by such methods are actually simple variants of a type of problem with which many of us are familiar from ordinary materials chemistry and crystallography.

Figure 1a shows a simple 1D chain of atoms in which the atoms are equally spaced. The distance between atoms is re-
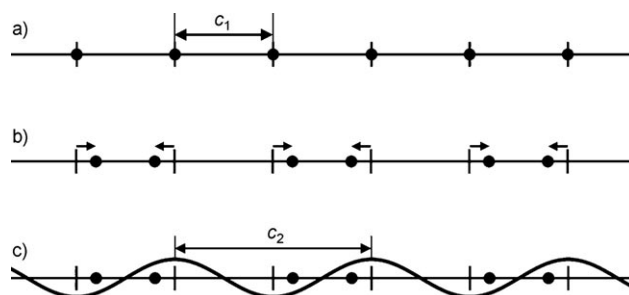


Figure 1. A simple 1D distorted system. a) Before distortion: all atoms (filled circles) lie equally spaced along a straight line. b) After distortion: half the atoms shift to the left, half to the right (arrows). c) Distortion in b) represented as a simple cosine function. Positive values of the function = atoms shifted left, negative values = atoms shifted right.

ferred to as $c_1$, the sole lattice parameter of the 1D unit cell. Figure 1b shows a distortion of this simple 1D chain of atoms. The atoms are shifted in the directions indicated by the arrows. The original atomic positions are indicated by hatch marks, and the atom positions after distortion are indicated by small solid circles. In Figure 1b, the atoms begin to form closely associated pairs. Many materials chemists would recognize this distortion as a Peierls distortion.[68–70]

---

[5] Cubic crystals are not listed in the Supporting Information. As we explain later in this article, cubic symmetry is incompatible with 4D crystallography, which is the focus of this article.

[6] It is also quite possible that some of the remaining structures may prove to be representations of higher-dimensional crystals, but of types hitherto not described.

# FOCUS REVIEWS

Although Figure 1b provides an adequate view of the distortion of a 1D chain of atoms, we found that an alternative view would be of greater utility. In this alternative view, we replaced the arrows of Figure 1b by simple curves such as the simple sinusoidal wave shown in Figure 1c. Positive values of this sinusoidal curve represent atoms that are shifted to the left, whereas negative values denote atoms that are shifted to the right.

With this convention in mind, we looked at all the places along the horizontal axis with hatch marks. We then moved the atoms that were originally located at these hatch marks either left or right, depending on the sign of the sinusoidal curve. As comparison of Figure 1b and c shows, the displacements generated by the sinusoidal curve of Figure 1c are the same as those denoted by the arrows in Figure 1b.

The cosine wave of Figure 1c has a wavelength $c_2$. As Figure 1 shows, $\frac{1}{2}c_2 = c_1$. However, much more complicated relations between $c_2$ and $c_1$ can and, as we shall see, do exist. In the next section, we consider the case whereby $c_1/c_2$ is not only not a simple number, it is not even a rational number. It is in cases like this that higher-dimensional crystallography becomes relevant.

## 4. The 1D Incommensurate Structure

Our introduction to higher-dimensional crystallography is multistepped. We look first at the simplest of all possible higher-dimensional systems, a system that involves a physical 1D chain of hypothetical atoms. In later sections new features will be added to this model by turning first to the 1D composite structure, then the 2D composite structure, and lastly real 3D composite systems (we will delve further into what composite systems are later). Finally, higher-dimensional Bravais classes will be discussed. At each step along the way we will become acquainted with key features of higher-dimensional crystallography. At the end of this article, our intention is that the reader would be able to use higher-dimensional crystallography in their own materials research projects.

### 4.1. Introduction to the 1D Incommensurate Structure

We begin our account of how to identify the higher-dimensional space group by examining how the higher-dimensional unit cell is created. Just as in ordinary 3D crystallography, the identification of higher-dimensional space groups requires initial determination of the unit-cell axes. To obtain the higher-dimensional unit-cell axes, we need to show how this unit cell is generated from an ordinary unit cell (an ordinary cell to which an extraordinary modification has occurred).

These ideas can be understood by considering the simplest of all possible crystalline systems: the one-dimensional crystal with a single atom per unit cell located initially at the unit-cell origin. This crystal was already shown in Fig-

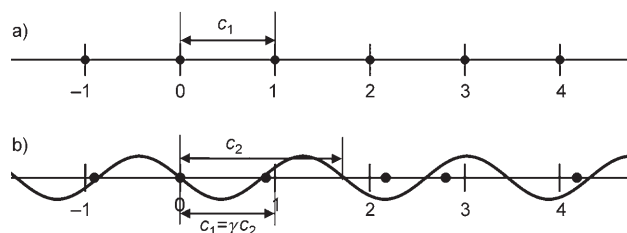ure 1a. We now consider a new variant of this structure (Figure 2).



Figure 2. A simple 1D incommensurate crystal. a) Before distortion: atoms (filled circles) lie equally spaced along a straight line. b) After distortion: atoms are displaced according to a periodic function. Positive values of the periodic function = atoms shifted left, negative values = atoms shifted right. The distorted structure is incommensurate as the wavelength of the periodic function, $c_2$, is not a rational multiple of the original unit-cell length $c_1$.

As discussed earlier, this simple crystal by itself is just a 1D crystal; it turns into a higher-dimensional crystal only after perturbation of its atomic positions. The perturbations are simple enough; as before, they follow a periodic function, and each atomic position is shifted according to the value of this periodic function at the original atomic position (indicated by hatch marks located at all integer values in Figure 2). The atom is moved according to the values of this function: positive values correspond to a shift to the left, negative values to a shift to the right (Figure 2b). Some useful terminology is as follows: the original atomic positions, at integer values, are given by the average position (or structure),[7] the atomic shifts are called the atomic displacements, and the final atomic positions are known as the real positions (or structure).

In the previous section, the perturbing function has a wavelength that is a simple multiple ($2\times$) of the original unit-cell length. In Figure 2, by contrast, something much more interesting happens. The perturbing wavelength $c_2$ is fundamentally different from the original unit-cell length $c_1$ (compare Figures 1 and 2). By fundamentally different we

---

[7] The average structure is clear in this case: it is the structure without atomic displacements. In general, as long as the displacements are small, identification of the average structure is fairly facile. We will give specific examples of the average structures and their determination throughout this article. Notably, the term "average structure" used herein is often spoken of as another concept, the basic structure. As defined above, the average structure is composed of the atomic positions in the small unit cell based on the average of the various modulated positions in the supercell structure. We feel that, for the general reader, the term "average structure" expresses more clearly and intuitively the averaging process by which the average structure is obtained in our hands. The attentive reader may also think that the average structure is not defined in a fully rigorous manner. As we hope to show in the examples herein, the average structure as we take it to mean leads in a practical manner to an accurate determination of the higher-dimensional structure and space group. All cases for which we have hitherto examined the concept of the average structure have led to a clear resolution of the higher-dimensional space group.

mean that the wavelength of the perturbing function is an irrational multiple of the original unit-cell length (why this can happen will be explained later in the text). As Figures 1 and 2 show, in such a case the rules by which the atoms are shifted seem much more complex.

In this new case, the atoms, which were all originally located at integral multiples of the unit-cell length, experience a different value of the perturbing function. Every atom is thus shifted by a slightly different amount to the others. The outcome is that the resulting atomic system is no longer a crystal; in the least, it is not a one-dimensional crystal.

This interesting system is called a 1D incommensurate structure. It comes about because the ratio of the perturbing wavelength $c_2$ to the original unit-cell length $c_1$ is an irrational number. This ratio is of sufficient importance to warrant its own name: we call it $\gamma$. Thus, $\gamma = c_1/c_2$, or $c_1 = \gamma c_2$ (Figure 2).

### 4.2. The (1+1)D Unit Cell

Although the system described in Figure 2b is not a 1D crystal, it is a cross-section of a 2D crystal. To show this, the following mathematical artifice is introduced. We rotate the perturbing periodic function of Figure 2b by 90°, not just once, but around every original atomic position (all at integral positions). This procedure is shown in Figure 3. The perturbing periodic function thus rotated crosses the original horizontal axis at the exact final (or real) positions of the atoms.

What is represented in Figure 3 is a crystal: a 2D crystal. This crystal has cell axes $\mathbf{x}_3$ and $\mathbf{x}_4$. (The length of the former axis is $c_2$. The length of the latter is discussed below.)
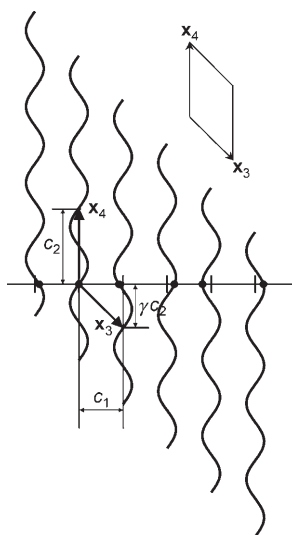


Figure 3. A simple 1D incommensurate structure represented as a 2D crystal. Atoms (filled circles) lie at the intersection of the horizontal line (the physical space) with a set of vertical periodic displacement functions. Drawn in this fashion, an oblique 2D unit cell with unit-cell vectors $\mathbf{x}_3$ and $\mathbf{x}_4$ can be discerned. Compare this figure with the conventional 1D representation of the simple 1D incommensurate structure given in Figure 2.

Interestingly, the crystal no longer contains points to describe atomic positions; rather, it uses periodic curved lines to denote the atomic positions. The final (or real) 1D incommensurate structure is the cross-section of this full 2D curved-line representation as it crosses the horizontal axis.

As the horizontal axis of the 2D crystal is the only portion of that crystal with any real physical meaning, it is possible to simplify the diagram in Figure 3 without changing its physical interpretation. In particular, as the vertical direction is completely perpendicular to the only physically real axis in the diagram, we can change the unit scale in the vertical direction at will. The easiest choice would be to change the vertical unit length so that $c_2$ is of length unity. As $c_2 = 1$, the expression $\gamma c_2$ in Figure 3 reduces to just $\gamma$, which is the ratio of the original unit-cell length $c_1$ to the perturbing wavelength $c_2$.

The 2D crystal thus simplified remains oblique (the 2D equivalent of a monoclinic crystal). Cell parameters are expressed by two cell-axis lengths and one cell angle. With reference to Figure 3 and some elementary trigonometry, the length of $\mathbf{x}_4$ is 1 and the length of $\mathbf{x}_3$ is $\sqrt{c_1^2 + \gamma^2}$. Similarly, the angle between these axes is $|\cot^{-1}(c_1/\gamma)|$.

We call this 2D crystal a (1+1)D crystal, not just because $1+1=2$, but because we wish to separate the number of physically real axes in the crystal (one, the first 1) from the number of physically unreal axes (also one in this example, the second 1) in the constructed crystalline system.

To understand the following sections, it is useful to note that the (1+1)D crystal shown in Figure 3 is not the only 2D crystal in which the horizontal cross-section is the perturbed 1D crystal structure in Figure 2b. We could also have chosen the new cell-axis direction not to lie perpendicular to the horizontal direction. Such a choice would have modified the overall picture.

In particular, as we want the real atomic positions to remain at the intersection of the wavy curves and the horizontal axes, we have to warp the shape of the former.[8] One useful direction for the curved lines is the $\mathbf{x}_3$ direction (Figure 4). Again, as only the horizontal portion of this crystal has real physical significance, we can define the wavelength of the curved lines at will. As shown later, for curved lines in the $\mathbf{x}_3$ direction, a useful choice for their wavelength is $\sqrt{c_1^2 + \gamma^2}$, which is the exact length we found previously for the $\mathbf{x}_3$ axis.

### 4.3. The 1D Composite Crystal

In the previous two sections, we considered a 1D crystal whose atoms are subject to the influence of a perturbing wavelength. This perturbing wavelength arises somewhat mysteriously from outside the original atomic positions. In this section, we consider a more immediate picture of the

---

[8] We do not have to warp the curves in Figure 3 as the vertical value of the curve is the exact amount by which the atoms are laterally displaced. A pure 90° rotation, therefore, converts the vertical value of the curve into the correct lateral displacement without change in functional shape. The same is not true for other directions.
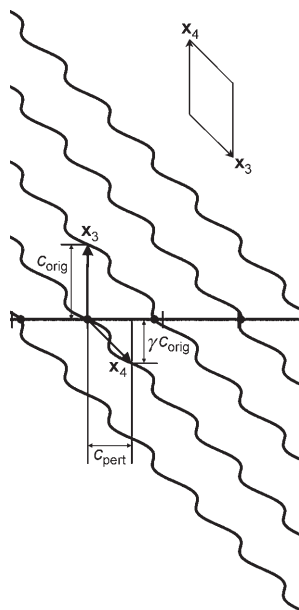
Figure 4. A simple 1D incommensurate structure represented as a 2D crystal. Atoms (filled circles) lie at the intersection of a horizontal line (the physical space) with a set of diagonal periodic displacement functions. Drawn in this fashion, an oblique 2D unit cell with unit-cell vectors $x_3$ and $x_4$ can be discerned. Compare this figure with the 2D representation shown in Figure 3. The 2D unit-cell parameters for both Figures 3 and 4 are the same.

perturbing wavelength (the example will need to be simplified, and will remain for now of a hypothetical nature).

In Figure 5, we consider a 1D system composed of two different atom types, represented in red and blue. As shown later, one atom type corresponds to a transition-metal atom, whereas the other is a main-group element. Both red and blue atoms originally lie by themselves in 1D unit cells, with both unit cells having only a single atom within them. The interesting complication of Figure 5 is that the unit-cell lengths of the red and blue atoms are fundamentally different from each other: that of the former is $c_1$ and that of the latter is $c_2$, where $c_1/c_2 = \gamma$, with $\gamma$ being an irrational number.

We now suppose that the red and blue atoms interact with one another. We could, for example, consider that red and blue atoms gently repel one another. As each atom type repels the other, it experiences a potential based on the positions of the atoms of the other type. The displacements that result from these potentials are shown in Figure 5a and c.[9] As in Figure 2, positive values of the displacement curves correspond to atomic shifts to the left, whereas negative values represent shifts to the right.

The fundamental assumption made is that the displacement curves are caused by the original positions of the atoms of the other chain. As a consequence, the displacement curves have the wavelength of the original unit cell of the other atom type. Thus, the displacement curve for the red atoms (red curve in Figure 5a) has wavelength $\lambda_1 = c_2$. Conversely, the displacement curves for the blue atoms (blue curve in Figure 5c) has wavelength $\lambda_2 = c_1$.

We can now combine Figures 3–5 into a single diagram. As in Figure 3, we rotate one displacement curve (the red curve of Figure 5a) so that it lies in the vertical direction. As in Figure 4, we rotate the other displacement curve (the blue curve of Figure 5) so that it lies in the $x_3$ direction. This combined diagram is shown in Figure 6a.

The resulting combination is the superposition of the two earlier curves, one on top of the other. The superimposed displacement curves of Figure 6a correspond to that of a single 2D crystal. The crossing of the red and blue curved lines of this 2D crystal (or more properly, (1+1)D crystal) with the horizontal axis gives the exact location of the red and blue atoms, respectively.

Also useful for later work is consideration of the average structure. The average structure is one in which both red and blue atoms lie unchanged from the potentials caused by the other atom type. It is the simple structure for which the displacement curves can be represented as flat lines (all displacements are equal to zero). The average structure represented as a (1+1)D crystal is shown in Figure 6b. Comparing Figure 6a and b, we see that the average structure (with no atomic displacements) has a unit cell of the same size as the (1+1)D crystal with atomic displacements.
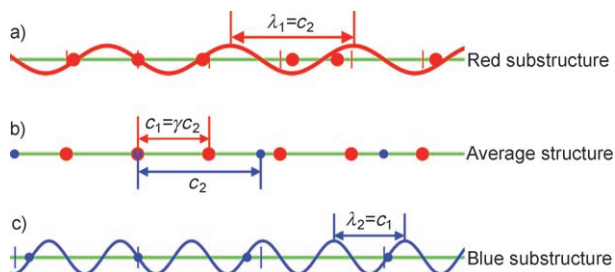


Figure 5. The 1D incommensurate composite system (b) made up of two separate incommensurate components (see Figure 2) superimposed onto each other. The two separate systems are shown in red and blue. The two component incommensurate systems are shown separately in a) and c). The periodic distortion of each component has a wavelength equal to the unit-cell length of the other component.

[9] One or both of the following points may have been noticed. First, displacements that result from the simple repulsive model posited herein should more properly have the shape of a tangent function: the non-analytical points of the tangent function, which tend toward $\infty$ when approached from the left and toward $-\infty$ when approached from the right, would correspond to the original location of the other atom type. In this article, we have drawn the displacement functions as simple sine curves, which is the simplest of all possible periodic functions. The sine curve was chosen because of the ease with which its general shape can be viewed and not for any physical reason. Second, the non-analytical points in the tangent function result from pairs of red and blue atoms that lie infinitely close to one another, for which repulsions would in principle become infinitely large. This is of course unreal. It turns out that in true physical systems, the two atom types (often transition-metal atoms vs. main-group atoms) lie in neighboring chains and, therefore, do not approach infinitely close to one another.
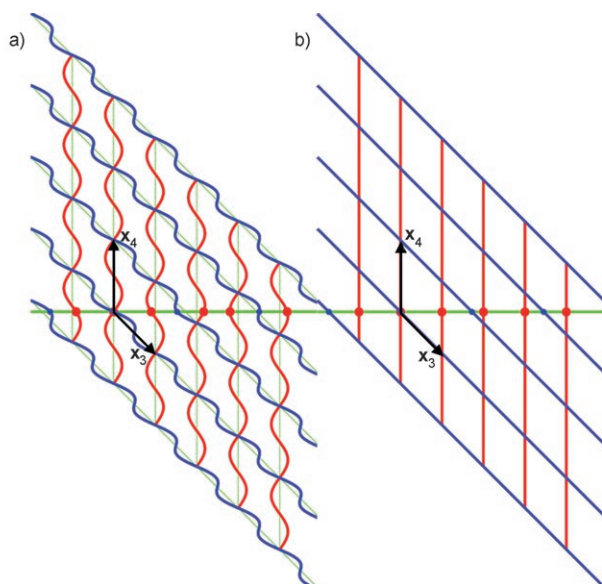
Figure 6. a) 1D incommensurate composite structure viewed as a 2D crystal. The atoms (red and blue filled circles) lie at the intersection of the horizontal axis (the physical space) with a series of vertical (red) and diagonal periodic curves (blue). This figure is a composite of Figures 3 and 4. b) 1D composite structure with no periodic distortion to the atomic positions. In b), the periodic curves of part a) are simplified to straight lines. Both a) and b) have the same 2D unit-cell parameters.
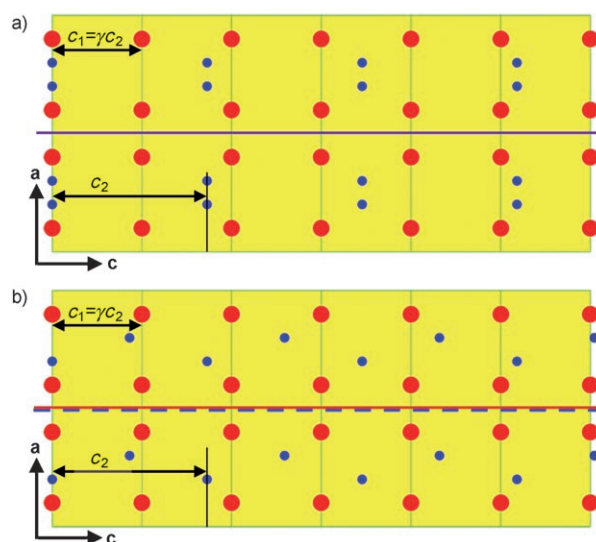


Figure 7. Two different 2D incommensurate composite structures. a) In this structure, both components (red and blue atoms; filled circles) share mirror-plane symmetry (solid purple line). b) In this structure, the red component has a mirror plane (solid red line), whereas the blue component has a $c$ glide (dashed blue line). Both composite structures are incommensurate in the $c$ direction but commensurate in the $a$ direction.

## 5. The 2D Composite Structure

In the preceding section, we considered the 2D (or more properly, the $(1+1)$D) representation of a 1D composite crystal. With this example, we learned the method by which a higher-dimensional crystalline unit cell can be fashioned from a lower-dimensional composite system. In this section, we move to a 3D system that is a $(2+1)$D composite crystal, that is, a physical 2D composite system that requires one additional nonphysical dimension to convert it into a crystalline representation. With this $(2+1)$D composite crystal in hand, we can study how actual space-group operations appear in higher-dimensional systems.

We consider first the system shown in Figure 7a. In this system, there are two types of atoms: red and blue. As in the preceding case, before displacement, the red and blue atoms lie in unit cells with only a single red or blue atom in them, respectively. As before, one interesting twist is that the unit cells of the red and blue atoms are not the same. Both unit cells are two-dimensional and bear the same $a$ axis, but the other cell axes, the $c_1$ and $c_2$ axes for the red and blue atoms, respectively, are fundamentally different from each other. In this latter case, the ratio of the two axes is again the irrational number $\gamma$. The $a$ axes are typically referred to as the common axis, whereas the $c_1$ and $c_2$ axes are denoted the incommensurate axes.

As Figure 7a shows, both the red and blue atoms share space-group symmetry elements. In particular, they share the mirror plane indicated in Figure 7a as a solid purple line. The standard crystallographic notation of a solid horizontal line to represent a mirror plane normal to the vertical direction is used here, and the color purple was chosen as it is made up of both red and blue. This mirror symmetry operation applies equally to the red and blue systems of atoms.

Simultaneously, we also consider the alternative chemical system shown in Figure 7b. This structure has exactly the same red-atom structure as that of Figure 7a, but it differs in the position of the blue atoms. Whereas the blue atoms in Figure 7a have mirror-plane symmetry, the blue atoms in Figure 7b have glide-plane symmetry ($c$ glide). In Figure 7b, the solid horizontal purple line of Figure 7a is therefore replaced by a solid horizontal red line (for the mirror plane of the red substructure) and a dashed horizontal blue line (for the glide plane of the blue system).

We now consider the displacements of the red and blue atoms caused by the composite nature of the crystals. We have seen in the previous section that the red and blue displacements can be expressed as curves, whose intersections with the physical axis gives the exact positions of the displaced atoms (Figure 5). Both the structures in Figure 7 differ from the previous example in that there are now two (rather than one) physical axes: the common $a$ axis and the incommensurate $c_1$ and $c_2$ axes. In these new cases, the red and blue atomic displacements are again represented respectively as red and blue curves, but now they need to intersect two physical axes to give the actual red and blue atomic positions.

The red and blue curves with the 2D physical structures are shown in Figure 8a and b. The red and blue curves run along the $\mathbf{x}_4$ and $\mathbf{x}_3$ directions, respectively, and the 2D physical structures are represented by the horizontal plane
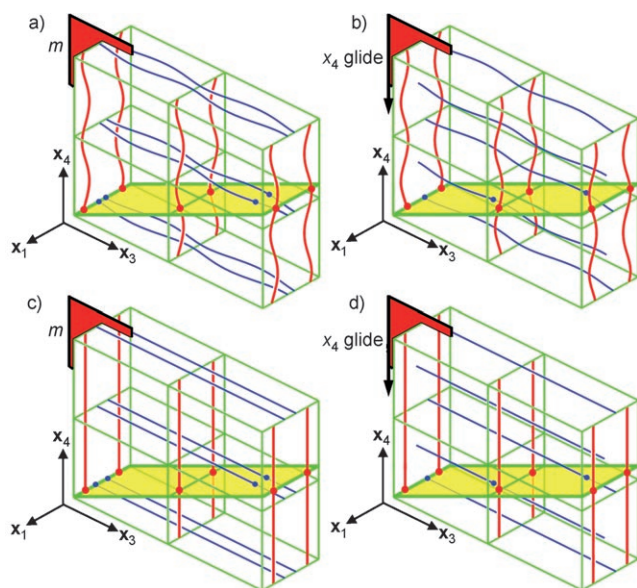
Figure 8. The two different 2D incommensurate composite structures of Figure 7 represented as 3D crystals. Atomic positions (filled circles) lie at the intersection of the horizontal plane (yellow; the physical space) with a series of periodic curves (red and blue). The structures of Figure 7a and b are represented by a) and b), respectively. The same structures are shown in c) and d) without periodic atomic distortions. Compare this figure with Figure 6.



Figure 9. Distortions of the two 2D incommensurate structures (see Figure 7) represented as "orbits" around the original undistorted atomic positions. Empty circles=undistorted atomic positions, filled circles=distorted atomic positions, large circles=distortions viewed as "orbits". The model drawn corresponds to repulsion between the red and blue atoms.



Figure 10. The 2D composite structure of Figure 7a represented in 3D space. As in Figure 8, the real 2D composite structure lies on a cross-sectional plane (which passes through the origin) normal to the $x_4$ direction. a) Unit cell viewed in the previously shown orientation of Figure 8. b) Unit cell viewed along the $x_3$ axis. The displaced atomic positions, which in the real 2D space lie in "orbits" around the undisplaced positions (see Figure 9), are represented in the 3D diagram as helices.

(shown in yellow). The red and blue curves intersect the yellow horizontal plane at the exact position of the red and blue atoms. Neither the red nor blue curve runs along the $x_1$ direction, because, as comparison of Figures 7 and 8 shows, $x_1$ points in the direction of the common $a$ axis.

As in the earlier example, it is useful to consider the 3D representation of the average structure, that is, the structure without atomic displacements. In the average structure, the red and blue curves degenerate into straight lines. These straight lines are shown in Figure 8c and d; the blue and red lines continue to run along the $x_3$ and $x_4$ directions.

### 5.1. Symmetry in the 2D Composite Structure

We now turn to a closer examination of the (2+1)D composite crystal of Figure 8a and b, with the goal of understanding the symmetry operations in this 3D system. We begin by examining the displacements of the red and blue atoms. We posit that both red and blue atoms shift away from each other toward the void spaces of the structure. As a consequence of this assumption, both red and blue atoms shift to positions that surround their original undisplaced positions (the so-called average positions).

Figure 9 illustrates these new atomic positions as orbits around their original undisplaced positions. If indeed atomic displacements correspond to a type of orbit around a central position, the curves based on these orbits, that is, the red and blue curves in Figure 8a and b, would actually be helices. These helices are shown explicitly in Figure 10. They
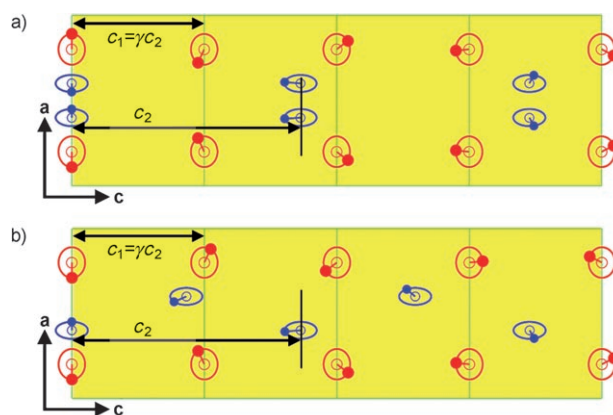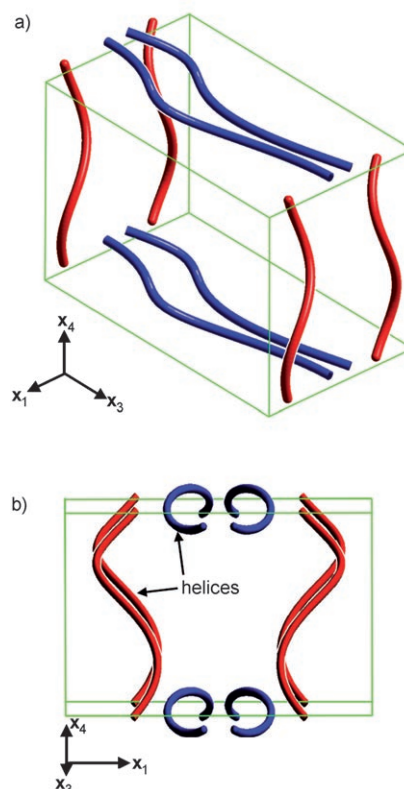
are the (2+1)D equivalent of the (1+1)D sine curves in the previous section.

We are now in a position to consider explicitly space-group symmetry operations. To find the space-group symme-

try, the symmetry relationship between the various red (and blue) helices must be identified. Close examination of Figure 8 is warranted. On the basis of our initial assumption that both red and blue atomic displacements are caused by atoms of the other color, it is the position of the curve of the other color that leads to the shape of the final helix.

The formation of the final helical shapes can be viewed as an evolutionary process that begins with the undisplaced positions of the original average structure. In the original average structure, the red and blue curves are straight lines (Figure 8c and d). In response to the other curve (blue or red), each curve begins to evolve by shifting away from places where the curves are in closest contact and toward places where the curves are far apart. The final result is the helices of Figure 9.

As the red and blue curves only experience a potential caused by the other curve, the displacements in the curves respect any space-group symmetries present in the other curve. If there is any space-group symmetry element present in the initial $(2+1)$D average structure, this symmetry element would be maintained throughout the evolution of the curve shapes. To identify the space-group symmetries of the $(2+1)$D system, we therefore need only identify the symmetry elements present in the original average structure itself.

As Figure 8c shows, there is a mirror plane normal to the $\mathbf{x}_1$ direction in the original average structure, shown in red. As anticipated by the above paragraph, this mirror plane remains in the final helical picture of Figure 8a. That the mirror plane is present at all is a direct consequence of its presence in both the red and blue substructures; it is originally shown as the purple horizontal line in Figure 7a (this point can be seen by particular attention to the yellow plane in Figure 8c, the physical structure, and its intersection with the red and blue lines running along the $\mathbf{x}_4$ and $\mathbf{x}_3$ directions, respectively). Written as a formula in standard crystallographic notation, this red mirror-plane operation can be expressed as $(\bar{x}_1, x_3, x_4)$: the point initially located at $(x_1, x_3, x_4)$ is thus transformed.

We now turn to Figure 8d, in which the mirror plane of Figure 8c is replaced by a glide plane. It is an $\mathbf{x}_4$ glide as the glide–translation is half a unit cell in the $\mathbf{x}_4$ direction. A comparison of Figures 7b and 8d shows that this glide operation comes about from the glide operation present in the blue substructure of Figure 7b. The glide operation in Figure 7b causes half the blue atoms to shift half a unit cell over. Consequently, half the blue lines of Figure 8d are shifted half a unit cell over, and the blue lines together take on a staggered appearance. The yellow plane (of Figure 8d) and its intersection with the blue lines is again of particular note. This glide plane is written mathematically and in standard notation as $(\bar{x}_1, x_3, x_4+\frac{1}{2})$.

In Figure 11, the symbols for the $(2+1)$D symmetry operations are shown explicitly below the diagrams of the two-dimensional composite systems. For good measure, an additional 2D composite system is included, in which the red-atom substructure has a glide plane but the blue a mirror plane (the converse of Figure 7b). In this latter case, consid-
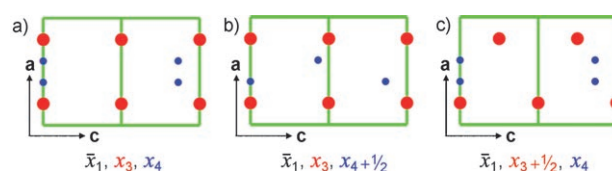


Figure 11. Illustration of rule that governs higher-dimensional space-group operations of composite structures: each composite component determines the space-group symbol for a different higher-dimensional cell direction. The red and blue components determine the $x_3$ and $x_4$ terms, respectively. Mirror and glide planes are represented as $x_3$ and $x_3+\frac{1}{2}$ (red component) and $x_4$ and $x_4+\frac{1}{2}$ (blue component). a) The red and blue components have mirror planes normal to the $a$ direction. b) The red component has a mirror plane, but the blue component has a glide plane. c) The red component has a glide plane, but blue component has a mirror plane. The mathematical expressions given under the respective structures all follow the stated rule.

eration of the 3D average structure shows the presence of an $\mathbf{x}_3$ glide plane (as this composite crystal is analogous to that of the previous cases, a full picture is not given here, unlike those in Figure 8). As Figure 11c states, this glide operation can be written as $(\bar{x}_1, x_3+\frac{1}{2}, x_4)$.

Figure 11 allows us to extract a general rule about higher-dimensional space-group operations. In the common directions of the crystal, the mathematical symmetry operation is unchanged from that of the original physical space. Thus, a mirror or glide plane normal to the $a$ direction causes (in all three cases) the first component of the symmetry operation to be $-x_1$, just as in ordinary crystallography.

Incommensurate directions are of even greater interest. As Figure 11 illustrates, the component of the first incommensurate direction, $\mathbf{x}_3$, is $x_3$ when the red substructure has a mirror plane, but is $x_3+\frac{1}{2}$ with a glide operation. Similarly, the component for the second incommensurate direction, $\mathbf{x}_4$, is $x_4$ when the blue substructure has a mirror plane, but is $x_4+\frac{1}{2}$ with a glide operation. In other words, the red substructure controls the mathematical operation in the $\mathbf{x}_3$ direction, whereas the blue substructure equally determines the operation in the $\mathbf{x}_4$ direction. For this reason, the mathematical symmetry components in Figure 11 are color-coded: red for values in the first incommensurate direction, blue for those in the second, and black for labels in the common $a$ direction.

It turns out that the result of Figure 11 is generally true: higher-dimensional symmetry operations can be found directly by considering the symmetry operations of the two substructures independently. Most importantly, in general, we need only consider the substructures in the original physical space. In this way, by examining the physical 2D diagram of the composite system in Figure 5b, the red and blue substructures are seen to have, respectively, a mirror plane $(\bar{x}_1, x_3)$ and a $c$ glide $(\bar{x}_1, x_4+\frac{1}{2})$ in the $a$ (or $\mathbf{x}_1$) setting, and that in this setting there is a $(2+1)$D space-group operation, $(\bar{x}_1, x_3, x_4+\frac{1}{2})$ (Figure 11).

This general rule is important for the remainder of this paper. Furthermore, this higher-dimensional symmetry has the same coordinates with respect to the common axis or

axes. We call this the principle of complementarity. This principle is of particular importance when we consider chemically real three-dimensional composite systems. Because of this rule, higher-dimensional symmetry elements can be deduced from the original physical 3D structures, and we only have to look at the 3D structures to deduce the (3+1)D (i.e., 4D) symmetry elements. Crystallographers are generally well-versed in viewing 3D structures; on the other hand, it is difficult to visualize 4D structures. Therefore, this general rule is a significant convenience in determining (3+1)D symmetry elements.

## 6. Real Intermetallic Composite Systems

### 6.1. Nowotny Chimney–Ladder Phases

#### 6.1.1. Nowotny Chimney–Ladder Phases as Composite Structures

As a first real example, we consider the Nowotny chimney–ladder (NCL) phases, a chiefly binary family of intermetallic compounds composed generally of main-group elements from Groups 13–14 and transition-metal atoms from Groups 4–9.[7–9,29,52–56,71,72] A typical example is $Ir_3Ga_5$,[29] which was discovered by Nowotny and co-workers 40 years ago (Figure 12).

At first glance, chimney-ladder structures such as $Ir_3Ga_5$ are complex. When the principal intermetallic bonds in the structure are drawn (bonds between Ir and Ga atoms; Figure 12a), it is hard to deduce much at all. However, when $Ir_3Ga_5$ is viewed as a composite structure, the overall crystal appearance is significantly simpler. The two components of the composite structure are the transition-metal network shown in red and the main-group network in blue and gray.

As Figure 12b shows, with respect to the transition-metal component, the unit cell is made up of three nearly equal transition-metal pieces (in red) stacked one on top of the other in the $c$ direction. Indeed, the axis length of the transition-metal component is $^1/_3$ that of the $c$ axis of the full composite structure. We call this length $c_L$; L stands for long (Figure 12). The structure of the main-group component is even simpler: it is a distorted chain of main-group atoms running along the $c$ direction. The blue (and equivalently the gray) atoms repeat roughly every $^1/_5$ of the full $c$ axis. As this is an even shorter distance than $c_L$, we call this length $c_S$, with S for short.

Figure 12 shows that the chains of main-group atoms form a fivefold helix, which when viewed down the $c$ axis nearly has the shape of a star. Unfortunately, the focus of this article is the identification of the higher-dimensional space group. As noted in the previous section, to determine this space group, we consider only the average structure, that is, the structure in which both main-group and transition-metal positions fully respect the translational symmetries of $c_S$ and $c_L$, respectively. The starlike shape of the main-group atoms is lost with respect to the $c_S$ unit cell. As there is only a single main-group atom in the $c_S$ cell, the average $c_S$ struc-
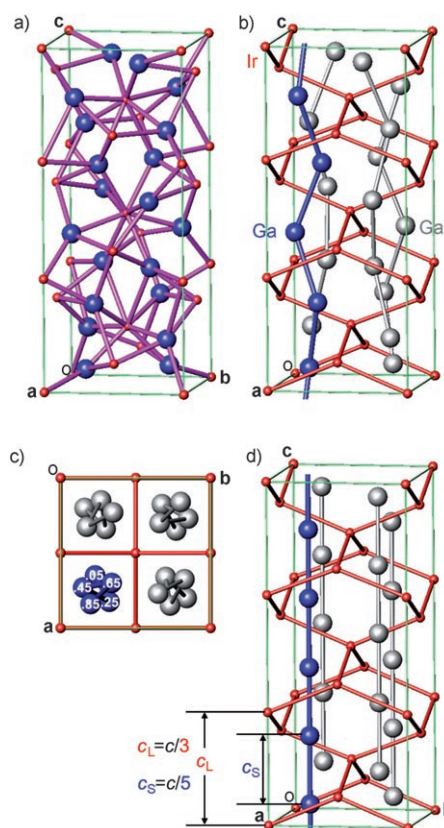


Figure 12. 3D composite structure of the Nowotny chimney–ladder phase $Ir_3Ga_5$. a) Structure with principal intermetallic Ir–Ga bonds shown. b) Structure considered as a composite of the Ir (red) and Ga substructures (gray and blue). c) Composite structure viewed along the $c$ axis. d) Each substructure has its own characteristic cell-axis parameter: $c_L$ and $c_S$ for the Ir and Ga components, respectively. The composite views given in b)–d) are visually simpler than the "bonding" view of a).

ture can contain just a linear chain of main-group atoms (Figure 12d).[10]

Nowotny chimney–ladder structures form a large range of conventional (commensurate) 3D crystal structures. Their stoichiometries, which include $Ru_2Sn_3$,[71] $Mn_4Si_7$,[73] $Cr_{11}Ge_{19}$,[55] $Mn_{15}Si_{26}$,[53] $Rh_{10}Ga_{17}$,[29] $Rh_{17}Ge_{22}$,[56] and $V_{17}Ge_{31}$,[55] as well as their range of $c$-axis lengths, which vary from 5 to over 100 Å, give some measure of their broad versatility. (Chimney–ladder structures with incommensurate cells are equally known.[7–9]) The conventional

---

[10] The key to choosing the average structure is to pick the substructure that has the highest symmetry compatible with the real atom positions. In going from the fivefold helix to the linear chain, we regain the four-fold axis of the original tetragonal system. Notably, when choosing the average substructure by the principle of complementarity, the real substructure results in general from the perturbations caused by the other substructure. In some cases, it is useful to consider other related phases that may share the same average substructure. For example, with NCL phases, whereas individual structures have different helices of main-group atoms (threefold for $Ru_2Sn_3$, sevenfold for $Mn_4Si_7$, or even 19-fold for $Cr_{11}Ge_{19}$), one readily arrives at the linear chain when searching for commonality between these structures, which is the only possibility compatible with the tetragonal symmetry of these systems.

space groups of these phases vary as well: for tetragonal chimney–ladder structures, the conventional cells break down into three separate space groups: $I\bar{4}2d$, $P\bar{4}c2$, and $P\bar{4}n2$.

Remarkably, despite all this variety, tetragonal Nowotny chimney–ladder phases, when viewed as composite crystals, have exactly the same type of average composite structures; the only differences are in the distances $c_L$ and $c_S$.[7–10] This observation leads to a real simplification. As shown in the following sections, the various tetragonal Nowotny chimney–ladder structures, even though they have different 3D space groups, may all belong to the same (3+1)D space group.

By way of motivation, we conclude this section by showing a simple illustration of the above assertion. The average structure of yet another chimney–ladder structure, $Ir_4Ge_5$,[72] is shown in Figure 13. Even though the space group of $Ir_4Ge_5$ is $P\bar{4}c2$, unlike $Ir_3Ga_5$, which has $P\bar{4}n2$ space-group symmetry, the average structures of these two compounds are quite similar, except for the different $c_S$ and $c_L$ distances.
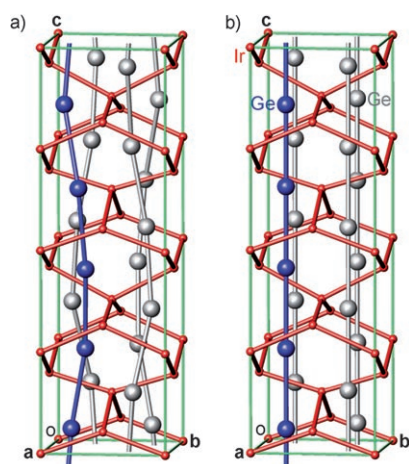


Figure 13. The Nowotny chimney–ladder phase $Ir_4Ge_5$. a) Actual structure showing two separate components. Red = Ir, blue and gray = Ge. b) Structure without atomic displacements caused by the other component. The structures a) and b) are termed the real and average structures, respectively. Compare the structure of $Ir_4Ge_5$ to that of $Ir_3Ga_5$ shown in Figure 12.

*6.1.2. (3+1)D Space-Group Symmetry in Nowotny Chimney–Ladder Phases*

In this section, we combine the results of the previous two sections. On the one hand is the analysis from the last section, that Nowotny chimney–ladder phases can be viewed as composite crystals. On the other is the general rule discussed two sections ago, that higher-dimensional space-group operations can be read directly from the space-group operations of the components.

Figure 14a shows the average structure of $Ir_3Ga_5$ viewed along the $c$ direction; this structure was previously viewed from another perspective (Figure 12d). (This average structure is equivalent to the average structure of other chimney–ladder phases.) In Figure 14b and c, we divide this per-
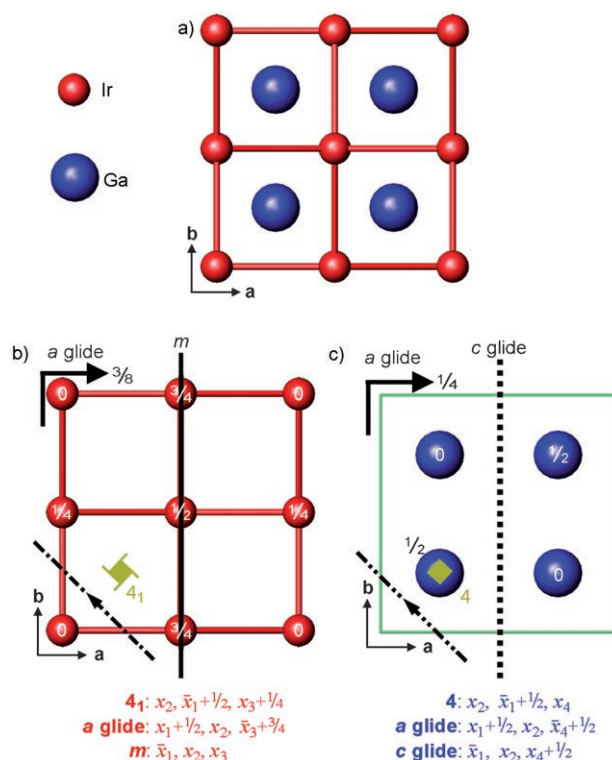


Figure 14. 3D symmetries of the Ir (red) and Ga (blue) components of the $Ir_3Ga_5$ composite structure. The structure is shown without atomic displacements due to the other component (see Figure 12). a) Structure viewed along the $c$ axis. b) The four generating symmetry operations of the Ir component ($4_1$, $a$ glide, $m$, and $d$ glide). c) The corresponding four symmetry operations for the Ge component. Explicit expressions for the first three generating operations are given under the respective figures. For the fourth, see Figure 15.

spective of the average structure into the transition-metal (red) and main-group (blue) components.

Each component on its own forms a crystalline lattice with a corresponding space group. We turn first to the transition-metal average network. A single unit cell of this network is given in Figure 14b. The cell is tetragonal and contains four atoms: at the cell corner, at the cell center, and at the center of both the $ac$ and $bc$ faces (the heights of the atoms in this figure are given with respect to the transition-metal $c$ axis, $c_L$; Figure 12); the cell is body-centered. Further examination of this cell shows that this substructure is of $I4_1/amd$ symmetry, space group No. 141 (this is the β-Sn structure[74] in solid-state chemistry).

There are 32 operations in this space group, all of which can be generated from the space-group elements mentioned in the space-group name: $I$, $4_1$, $a$, $m$, and $d$. In this section, we restrict our attention to space-group operations that are not centering conditions (i.e., do not pertain to the Bravais lattice type); we therefore turn to the last four operations. In Figure 14b, the $4_1$, $a$, $m$, and $d$ operations are represented by using their standard crystallographic symbols; each of these symmetry operations are indeed found in this structure.

Even more interesting is the main-group average network shown in blue in Figure 14c. There are four atoms in the unit cell: two at height zero and two at height $\frac{1}{2}$. Heights here are given with respect to the main-group $c$ axis, that is, $c_S$ of Figure 12. The space-group operations of the main-group structure are drawn explicitly in Figure 14c. But rather than placing a canonical set of generating space-group operations, we consider instead those main-group space-group operations that have the same rotation or reflection component as the previous $4_1$, $a$, $m$, and $d$ operations of the transition-metal average network (i.e., symmetries that are complementary to the transition-metal network). As Figure 14c shows, the $4_1$, $a$, and $m$ operations of the transition-metal network are replaced, respectively, by a fourfold rotation, an $a$ glide, and a $c$ glide. Either the new symbols are different, or, in the case of the $a$ glide, one component of the glide has changed. In the transition-metal network, the mirror reflection of the $a$ glide lies at height $\frac{3}{8}$, whereas in the main-group network, it is at height $\frac{1}{4}$.

We turn now to the last of the four generating space-group operations of the transition-metal component, the $d$ glide. This diamond-glide operation transforms in a most unusual manner when shifted to the main-group component. The reflection part of this symmetry operation must, by the principle of complementarity, remain the same. The unusual features lie in the translation part of this glide operation. Whereas, for the transition-metal component, the translation part of the diamond glide is the standard $(\frac{1}{4}, \frac{1}{4}, \frac{1}{4})$ shift, for the main-group component, the glide–translation is a nonstandard $(\frac{1}{4}, \frac{1}{4}, \frac{1}{2})$ shift. This main-group glide–translation has neither an ordinary glide name nor a standard crystallographic symbol. With reference to Jana2000,[75,76] it is termed a $g_2$ glide. We therefore coined the symbol shown in Figure 14c (this symbol was chosen to resemble an ordinary diamond-glide operation, but has twice as many dots than a diamond glide to indicate that the fractional shift in the $c_S$ direction is double that of a normal diamond operation).

Figures 14 and 15 show explicitly the mathematical formulae of the transition-metal $4_1$, $a$, $m$, and $d$ operations and their main-group counterparts. Thus, the transition-metal $4_1$ and the main-group fourfold axes are written as $(x_2, \bar{x}_1+\frac{1}{2}, x_3+\frac{1}{4})$ and $(x_2, \bar{x}_1+\frac{1}{2}, x_4)$, respectively. Two sections ago, we noted that one could directly express the higher-dimensional space-group operations from knowledge of the physical space-group operations. The rule discussed previously was that for the higher-dimensional operations, the common-axis coordinates (i.e., in the $a$ and $b$ directions; in other words, the $\mathbf{x}_1$ and $\mathbf{x}_2$ directions) remain the same, but two new additional axes are included (one for each component). The two new coordinates are $\mathbf{x}_3$ and $\mathbf{x}_4$, which refer to the transition-metal and the main-group incommensurate components, respectively. Applying this rule to the $4_1$ and fourfold operations, we derive from the two initially separate three-dimensional operations $(x_2, \bar{x}_1+\frac{1}{2}, x_3+\frac{1}{4})$ and $(x_2, \bar{x}_1+\frac{1}{2}, x_4)$ a single $(3+1)D$ space-group operation, $(x_2, \bar{x}_1+\frac{1}{2}, x_3+\frac{1}{4}, x_4)$.
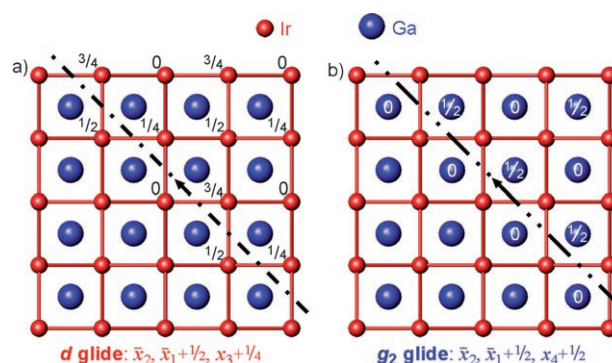


Figure 15. a) The $d$ glide of the Ir (red) component and b) the corresponding symmetry operation for the Ga (blue) component of the $Ir_3Ga_5$ composite structure. The structure is shown without atomic displacements due to the other component (see Figures 12 and 14). Explicit expressions for these two symmetry operations are given under the respective figures. These symmetry operations are one of the generating operations of the 3D space group for the Ir and Ga components.

In the same manner, the mathematical formulae for the other 3D space-group operations (given in Figures 14 and 15) can be combined to obtain the correct $(3+1)D$ space-group operations. These are given in Table 3. As stated in this table, the $(3+1)D$ replacement for the $a$, $m$, and $d$ operations are $(x_1+\frac{1}{2}, x_2, \bar{x}_3+\frac{3}{4}, \bar{x}_4+\frac{1}{2})$, $(\bar{x}_1, x_2, x_3, x_4+\frac{1}{2})$, and $(x_2, \bar{x}_1+\frac{1}{2}, x_3+\frac{1}{4}, x_4+\frac{1}{2})$, respectively.

Table 3. Generation of rotoreflection symmetries for Nowotny chimney–ladder phases.

| Symmetry | $x_1$ | $x_2$ | $x_3$ | $x_4$ |
|---|---|---|---|---|
| **Transition-metal network** | | | | |
| $4_1$ | $x_2$ | $\bar{x}_1+\frac{1}{2}$ | $x_3+\frac{1}{4}$ | |
| $a$ | $x_1+\frac{1}{2}$ | $x_2$ | $\bar{x}_3+\frac{3}{4}$ | |
| $m$ | $\bar{x}_1$ | $x_2$ | $x_3$ | |
| $d$ | $\bar{x}_2$ | $\bar{x}_1+\frac{1}{2}$ | $x_3+\frac{1}{4}$ | |
| **Main-group network** | | | | |
| $4_1$ | $x_2$ | $\bar{x}_1+\frac{1}{2}$ | | $x_4$ |
| $a$ | $x_1+\frac{1}{2}$ | $x_2$ | | $\bar{x}_4+\frac{1}{2}$ |
| $c$ | $\bar{x}_1$ | $x_2$ | | $x_4+\frac{1}{2}$ |
| $g_2$ glide | $\bar{x}_2$ | $\bar{x}_1+\frac{1}{2}$ | | $x_4+\frac{1}{2}$ |
| **Transition-metal network** | | | | |
| $4_1$ | $x_2$ | $\bar{x}_1+\frac{1}{2}$ | $x_3+\frac{1}{4}$ | $x_4$ |
| $a$ | $x_1+\frac{1}{2}$ | $x_2$ | $\bar{x}_3+\frac{3}{4}$ | $\bar{x}_4+\frac{1}{2}$ |
| $m$ | $\bar{x}_1$ | $x_2$ | $x_3$ | $x_4+\frac{1}{2}$ |
| $d$ | $\bar{x}_2$ | $\bar{x}_1+\frac{1}{2}$ | $x_3+\frac{1}{4}$ | $x_4+\frac{1}{2}$ |

We are now very close to our goal of determining the higher-dimensional space-group symbol (except for the Bravais lattice type). Before that, there is one further point that must be considered. Fortunately, it can be understood in the context of regular 3D crystals. For this issue, the fractions $\frac{1}{4}$, $\frac{1}{2}$, and $\frac{3}{4}$, which appear in the mathematical formulae of the space-group operations shown above, must be examined more carefully.

As we shall see, just as in ordinary 3D crystallography, the origin of these fractions stem from two separate sources.

The first is the translational components of glide planes (or screw axes). The second has nothing to do with the glide operation, but rather that the symmetry operation in question does not pass through the origin of the unit cell. The first source is therefore a fixed feature of the space group, and the second pertains to the unit-cell origin.

We give a 3D example here. Let us consider an *a* glide whose mirror plane is normal to the *c* axis and assume that the mirror plane of this glide passes through the origin of the unit cell, that is, it lies in the *ab* plane at height $c = 0$. Such an operation would be expressed as $(x_1 + \frac{1}{2}, x_2, \bar{x}_3)$. The fraction $\frac{1}{2}$ that appears in this expression refers to the translational component of the *a* glide.

Let us now consider instead an *a* glide whose mirror plane is still normal to the *c* axis, but does not pass through the origin; instead, it lies at height $c = \frac{1}{4}$. In other words, the mirror plane has the same orientation as the mirror plane of the previous paragraph, but lies at a different height. In this case, the glide operation is represented as $(x_1 + \frac{1}{2}, x_2, \bar{x}_3 + \frac{1}{2})$. Here, the first $\frac{1}{2}$ in this expression refers to the glide component of the translation, whereas the second $\frac{1}{2}$ refers to a shift in the height of the mirror plane.

The names of $(3+1)$D space groups distinguish between these two possibilities. The space-group name explicitly recognizes fractions due to translational components, but does not consider fractions due to the different possible origins of the unit cell. In applying this rule, particular attention is paid to the second component of the composite structure (in the case of Nowotny chimney–ladder phases, the main-group atoms form the second component). For this component, we examine space-group operations that correspond to the generating space-group operations of the first (transition-metal) component. As discussed previously, these main-group operations are a fourfold rotation, an *a* glide, a *c* glide, and a $g_2$ glide. Only the *c* and $g_2$ glides have fractional components of glide–translation in the $x_4$ direction (i.e., the incommensurate direction) (Figures 14 and 15). In both cases, the fraction is $\frac{1}{2}$, a number represented in the International Tables Volume C by the letter *s* (the fractions $\frac{1}{3}$, $\frac{1}{4}$, and $\frac{1}{6}$ are represented by the letters *t*, *q*, and *h*, respectively).[23]

The space-group names for the generating operations of the Nowotny chimney–ladder phases can now be stated explicitly as $4_1/amd(00ss)$ The origin of the name is as follows: $4_1/amd$ refer to the symmetry operations of the first (transition-metal) component. We know these letters are correct because we know that the 3D space group for the first component is $I4_1/amd$. The second part of the symbol, $(00ss)$, refers to the second component. For the second component, we know that the rotoreflection portion of the space-group operations must be the same as for the first component. Information about the rotoreflection portion of the operations is therefore wholly contained in the $4_1/amd$ part of the space-group name, and we need consider only the translational portions of the space-group operations of the second component. As discussed above, the four second-component generating operations are $4/acg_2$. Of these, only the last two

have fractional glide–translation components along the incommensurate *c* direction. Hence, the first two operations (4 and *a* glide) are designated the symbol 0 (i.e., no glide–translation component in the $x_4$ direction), whereas the latter two operations (*c* and $g_2$ glide) carry the letter *s* (i.e., a $\frac{1}{2}$ glide–translation fractional component). The generating operations of the $(3+1)$D space group are therefore designated $4_1/amd(00ss)$.

## 7. The $(3+1)$D Bravais Lattice

### 7.1. An Elementary Example

The determination of the remaining part of the $(3+1)$D space-group name requires the determination of the $(3+1)$D Bravais classes. This is carried out with an approach quite similar to that used for determining $(3+1)$D rotoreflection symmetry elements. The crux of the method is to examine the individual 3D substructures of a composite structure separately, determine their 3D symmetry elements, and only then apply the principle of complementarity to join these elements together into full-fledged $(3+1)$D symmetry operations.

In the earlier sections, our attention was focused on rotations and reflections (e.g., the $4_1/amd$ and $4/acg_2$ symmetries of the respective substructures of Nowotny chimney–ladder phases). We now turn to 3D translational symmetry and, hence, 3D Bravais classes. We begin with an elementary example: the structure of Rb-IV at a pressure of 17–20 GPa.[25,26,77] Although high-pressure Rb-IV has only one type of element, its structure, remarkably, is most conveniently viewed as having two tetragonal substructures with a common *a* axis of 10.35 Å but different *c* axes ($c_1 \approx 5.19$, $c_2 \approx 3.18$ Å).[11]

The structure of Rb-IV is illustrated in Figure 16 and is divided into two substructures: the first substructure, in red, is on the left, whereas the second substructure, in blue, is on the right (both red and blue atoms are, of course, rubidium atoms). Atom heights of the different rubidium atoms are also shown. The fractional heights of the red and blue atoms in this figure are with respect to the $c_1$ or $c_2$ axes and therefore cannot be directly compared with one another.

The two substructures can be separately described: the red substructure consists of two rosettes of atoms, one centered at the cell corner and the other at the cell center. These rosettes are arranged in a body-centered fashion. The blue substructure is even simpler: there are just two atoms in the unit cell, located in a body-centered manner.

It is easy to write the fundamental 3D lattice vectors (the generating vectors of the Bravais lattice) of these two cells. We wish, however, to use a single canonical procedure to obtain the generating vectors of any given Bravais lattice. The convention adopted herein is to specify only three generating vectors per 3D Bravais lattice. First, all lattice vec-

---

[11] In this, rubidium is hardly alone. To our knowledge so far, seven other elements adopt composite structures at high pressure: K, Sr, Ba, Sc, As, Sb, and Bi.[28,77]
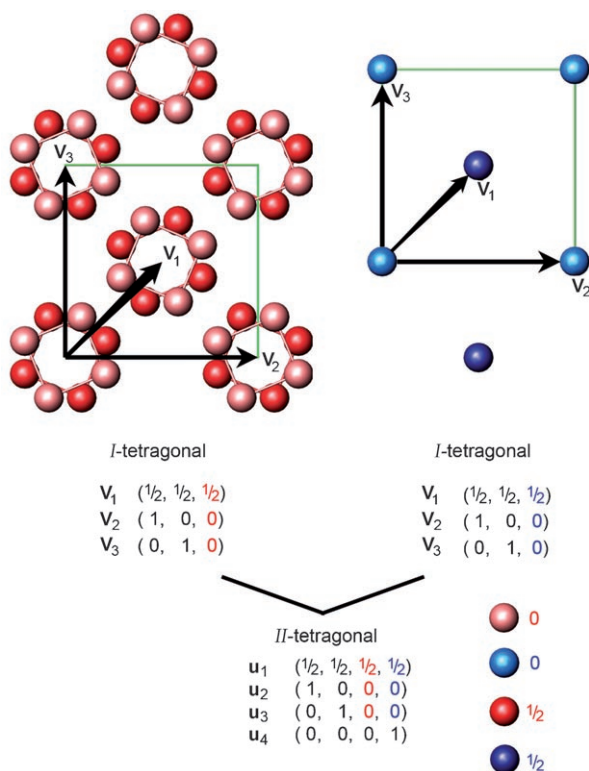
Figure 16. (3+1)D Bravais lattice for the composite structure of high-pressure Rb-IV. From the two component average substructures (top), the 3D Bravais lattice generating vectors can be derived (middle). By the principle of complementary, (3+1)D vectors are formed from the fusion of two 3D vectors (the third component of the (3+1)D vectors derives from the vectors of the red substructure, the fourth from those of the blue). A fourth vector, (0, 0, 0, 1), is added to complete the 4D space.

tors that correspond to centering conditions are included as one of the three required operations. Thus, in the case of an $I$-centered cell, the translation $(^1/_2, ^1/_2, ^1/_2)$ is included. The remaining generating operations are then chosen sequentially from the $a$, $b$, and $c$ directions.[12]

For the case of Rb-IV, the canonical 3D generating vectors of the red and blue substructures are the vectors $\mathbf{v}_1$, $\mathbf{v}_2$, and $\mathbf{v}_3$ (Figure 16). At first glance, the three generating vectors of both substructures look identical. However, although $\mathbf{v}_1$ for the two substructures may look the same, they are not. Here, $c_1 \neq c_2$, hence the $^1/_2 c$ coordinates of the two $\mathbf{v}_1$ vectors refer to different $c$ translations. By contrast, $a_1 = a_2 = a$ and $b_1 = b_2 = b$, thus the $^1/_2$ in the $a$ and $b$ coordinates refers to exactly the same $a$ and $b$ translations. This is an important distinction.

We can say that the red and blue $\mathbf{v}_1$ vectors are complementary to each other as their coordinates are exactly the same with respect to the $a$ and $b$ axes (the common axes). For two vectors to be complementary, the vector coordinates

in the third direction, the incommensurate axes, are of no matter: in the third direction, the coordinates may be equal or not. As Figure 16 shows, each of the pairs of $\mathbf{v}_1$, $\mathbf{v}_2$, and $\mathbf{v}_3$ vectors are complementary.

The 3D-lattice generating vectors of the two substructures are in the same type of complementary relationship with one another; this was previously found when we examined the rotoreflection symmetry elements of the two substructures of a given composite structure. Thus, for example, when we considered the $4_1$ and fourfold axes of the two substructures in Nowotny chimney–ladder phases, we noted that the two operations $4_1$, $(x_2, \bar{x}_1 + ^1/_2, x_3 + ^1/_4)$, and 4, $(x_2, \bar{x}_1 + ^1/_2, x_4)$ are complementary, for which the common axis coordinates of these two operations are the same, but the incommensurate axes coordinates could be different.

We can therefore treat the pairs of $\mathbf{v}_1$, $\mathbf{v}_2$, and $\mathbf{v}_3$ vectors of the red and blue substructures in a manner identical to that used in the case of rotoreflections. In those earlier systems, we combined the two 3D operations into a (3+1)D operation. The first two coordinates are those with respect to the common axes, and the third and fourth coordinates are taken from the incommensurate coordinates for the red and blue substructure, respectively. We apply this same procedure here for the $\mathbf{v}_1$, $\mathbf{v}_2$, and $\mathbf{v}_3$ vectors. The resulting (3+1)D vectors are shown in Figure 16.

In the procedure outlined above, we generated three fundamental lattice vectors for the (3+1)D Bravais lattice. Only one more (3+1)D vector is required to generate the full lattice. Given that the fourth dimension of the (3+1)D Bravais lattice is a mathematical artifice, this fourth Bravais lattice vector should be chosen to be as simple as possible. The simplest fourth vector is (0, 0, 0, 1), and this proves to be an adequate fourth vector in all cases (this vector is the combination of (0, 0, 0) in the first substructure and (0, 0, 1) in the second substructure). We include this fourth vector in Figure 16.

We call these four fundamental lattice vectors $\mathbf{u}_1$, $\mathbf{u}_2$, $\mathbf{u}_3$, and $\mathbf{u}_4$. All (3+1)D Bravais lattice vectors can be generated from integral combinations of these vectors. Hence, these four vectors can be considered to be the four canonical generating operations of the (3+1)D Bravais lattice.

It would be useful, however, if we could adopt a simpler notation that captures the information given by these four Bravais lattice generating lattice vectors, in much the same way that ordinary $I$-centering represents the three 3D generating lattice vectors $(^1/_2, ^1/_2, ^1/_2)$, (1, 0, 0), and (0, 1, 0). We propose here a simple labeling scheme. By the prescriptions given above, the fact that both the red and blue substructures are $I$-centered tetragonal specifies all the information necessary to determine $\mathbf{u}_1$, $\mathbf{u}_2$, $\mathbf{u}_3$, and $\mathbf{u}_4$. We therefore call the (3+1)D Bravais lattice $II$-tetragonal, whereby the first and second $I$ symbols refer to the red- and blue-substructure Bravais lattice, respectively.

This general approach appears promising. With only knowledge of the 3D Bravais lattices of the two substructures, one can obtain the (3+1)D Bravais lattice, which is described by placing the two 3D Bravais lattice symbols one

---

[12] We may follow this prescription in all cases except for a $C$-centered cell. In this case, the vectors $(^1/_2, ^1/_2, 0)$ and the $a$ and $b$ directions span only a 2D space. Therefore, for a $C$-centered cell, we choose as our three generating translations the vector $(^1/_2, ^1/_2, 0)$ and the $b$ and $c$ directions.

after the other. This is the simplest notation for the (3+1)D Bravais lattice we know of. There are, however, a number of complications that need to be considered, and we do so below.

### 7.2. A General Procedure for (3+1)D Bravais Lattices

From the discussion in the last section, we found that, to obtain the (3+1)D Bravais lattice, we only need to determine the two 3D Bravais lattices of the two substructures. For example, the first and second substructures of Rb-IV are both *I*-centered tetragonal, so the Rb-IV (3+1)D Bravais lattice can be correctly specified by the symbol *II*-tetragonal. This procedure, however, needs to be examined more closely if we are to have a general procedure for determining (3+1)D Bravais lattices. Nowotny chimney–ladder phases, a set of compounds considered earlier in this article, are an ideal starting point for this examination.

We begin, just as we did in the case of Rb-IV, by specifying the two substructures in Nowotny chimney–ladder phases. The first substructure, based on the transition-metal atoms, is shown in red in Figure 17; the second substructure, based on the main-group atoms, is given in blue. We examine both substructures separately for their individual Bravais lattice vectors. A few of these vectors, $\mathbf{v}_1$–$\mathbf{v}_5$, are shown in Figure 17.

A difference can immediately be seen between the Nowotny chimney–ladder phases and the Rb-IV structure. In the latter, the Bravais lattice vectors of each substructure are in a complementary relationship with a Bravais lattice vector of the other substructure. By contrast, for the Nowotny chimney–ladder phases, although there is a complementary blue Bravais lattice vector for each red vector, the converse is not true. Thus, whereas the red and blue substructures have complementary red and blue vectors $\mathbf{v}_1$, $\mathbf{v}_2$, and $\mathbf{v}_3$, there is no complementary red vector for the blue vectors $\mathbf{v}_4$ and $\mathbf{v}_5$.

However, complementarity is the abiding principle that underlies (3+1)D symmetry operations. Simply put, only pairs of symmetry operations that are complementary can be used to generate higher-dimensional symmetry operations. In the case of Bravais lattices, the solution is simple: we ignore all Bravais lattice vectors that do not have a complementary vector in the other substructure. Thus, we exclude, among others, $\mathbf{v}_4$ and $\mathbf{v}_5$, but we keep the vectors $\mathbf{v}_1$, $\mathbf{v}_2$, and $\mathbf{v}_3$. These restricted sets of complementary vectors are shown in the middle of Figure 17.

The middle panel of Figure 17 reveals a further important point: both restricted sets are still 3D Bravais lattices (we call these the restricted red and blue Bravais lattices). For the first substructure, the restricted Bravais lattice is still *I*-centered; for the second, the restriction of complementarity reduced the second Bravais lattice to a *P*-centered lattice (this *P*-centered lattice has different cell parameters from the first substructure: $\mathbf{a}_2 = (\mathbf{a}_1 - \mathbf{b}_1)/2$ and $\mathbf{b}_2 = (\mathbf{a}_1 + \mathbf{b}_1)/2$).

As with the case of Rb-IV, we now combine the two restricted 3D Bravais lattice vectors and, with the procedure
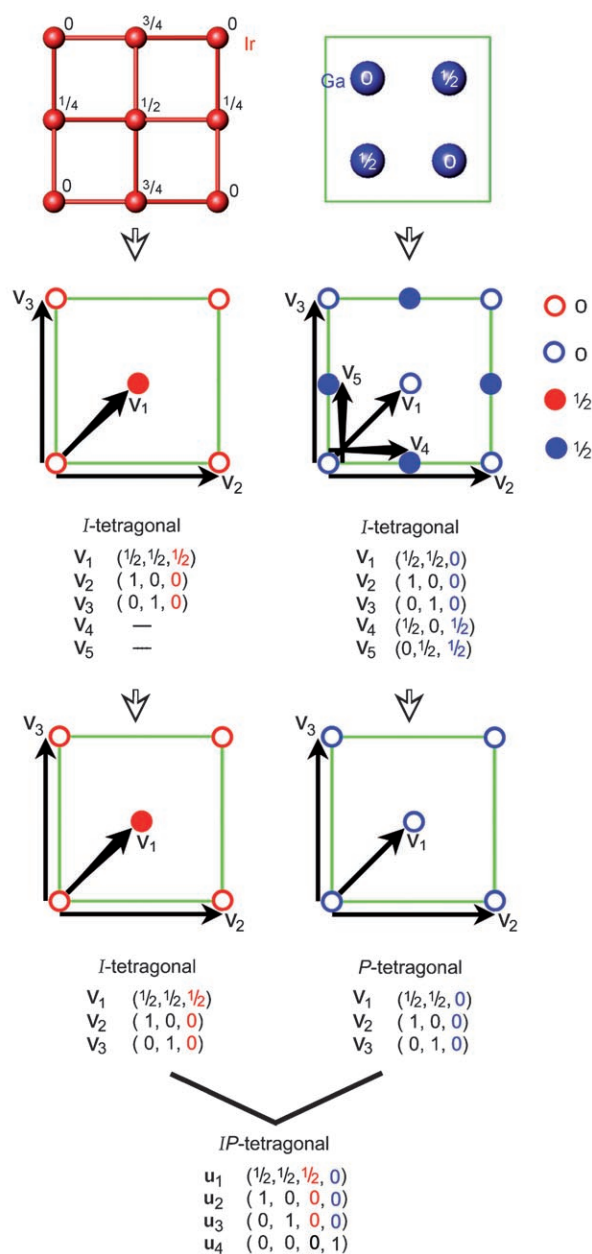


Figure 17. (3+1)D Bravais lattice of Nowotny chimney–ladder phases. The two average substructures are given in red and blue (top). The average substructure of the 3D Bravais lattices and their vectors are given in the middle panel. The blue substructure has Bravais lattice vectors for which there are no complementary vectors in the red substructure ($\mathbf{v}_4$ and $\mathbf{v}_5$). Those Bravais lattice vectors that have a complementary vector in the other average substructure are fused together to form a (3+1)D set. (The vector (0, 0, 0, 1) is added to complete the set.) The result is a (3+1)D *IP*-tetragonal Bravais lattice (bottom).

outlined in the previous section, generate the (3+1)D Bravais lattice. The generating vectors for this (3+1)D Bravais lattice are given in Figure 17 as $\mathbf{u}_1$–$\mathbf{u}_4$. By using the nomenclature developed for Rb-IV but by applying it only to the restricted Bravais lattices, the (3+1)D Bravais lattice is found to be *IP*-tetragonal.

### 7.3. Tetragonal (3+1)D Bravais Lattices

The examples of the last two sections give us a general procedure for obtaining (3+1)D Bravais lattices. It has four steps: 1) find the 3D Bravais lattice vectors for each 3D substructure separately, 2) delete those lattice vectors that have no complement in the other substructure (i.e., find the two restricted Bravais lattices), 3) specify the canonical generating lattice vectors for the first 3D substructure and find the complementary vectors for this canonical set for the second substructure, and 4) combine the two sets of vectors to obtain the (3+1)D Bravais lattice.

This procedure is sufficiently convoluted for specifying concretely the different complementary restricted Bravais lattices and their resultant (3+1)D Bravais lattice types. In this section, we do so for (3+1)D tetragonal structures. We begin by noting that all 3D Bravais lattices are of either *I*- or *P*-type. We therefore only need consider these two types of 3D cells.

In the simplest case, the 3D Bravais lattices are both the same. Both could be *P*- or *I*-centered. The resultant (3+1)D cells in these two cases would be *PP*- or *II*-tetragonal, respectively. Slightly more complex is the case whereby the two substructures still share the same *a* and *b* axes, but one of the substructures is *I*-centered while the second is *P*-centered. This case is illustrated in Figure 18.

According to the procedure outlined in the previous section, we restrict our attention to those Bravais lattice vectors that have a complement in the other substructure. This restricted set of vectors is illustrated in the middle panel of Figure 18. As this figure shows, the restricted Bravais lattices are both of *P*-type. The resultant (3+1)D Bravais is, therefore, *PP*-tetragonal.

At first glance, we might think that the above list exhausts all possibilities for (3+1)D Bravais lattices. But there are, in fact, other possibilities. We can, for instance, have an *I*-centered first substructure and a *P*-centered second substructure, but for which the two *a* and *b* axes are not equal. As Figure 19 shows, if the unit cell of the second substructure is rotated by 45° with respect to the first substructure and, additionally, $\mathbf{a}_2 = (\mathbf{a}_1 - \mathbf{b}_1)/2$ and $\mathbf{b}_2 = (\mathbf{a}_1 + \mathbf{b}_1)/2$, there is a one-to-one complement for each and every Bravais lattice vector. As Figure 19 shows, the (3+1)D Bravais lattice is *IP*-tetragonal.

The final case for which a natural one-to-one correspondence can be established is the case whereby the first substructure is *P*-centered and the second substructure is *I*-centered and, additionally, $\mathbf{a}_2 = \mathbf{a}_1 - \mathbf{b}_1$ and $\mathbf{b}_2 = \mathbf{a}_1 + \mathbf{b}_1$ (Figure 20). The resultant (3+1)D Bravais lattice is, therefore, *PI*-tetragonal. The *IP*-tetragonal case of Figure 19 and the *PI*-tetragonal case of Figure 20 are nearly the same, but the roles of first and second substructures have been transposed. Notably, even though this is true, the (3+1)D generating vectors are not related by a simple transposition.

A natural question at this point is whether there are additional pairs of tetragonal 3D Bravais lattices that must also be considered. The answer to this question is no. Although
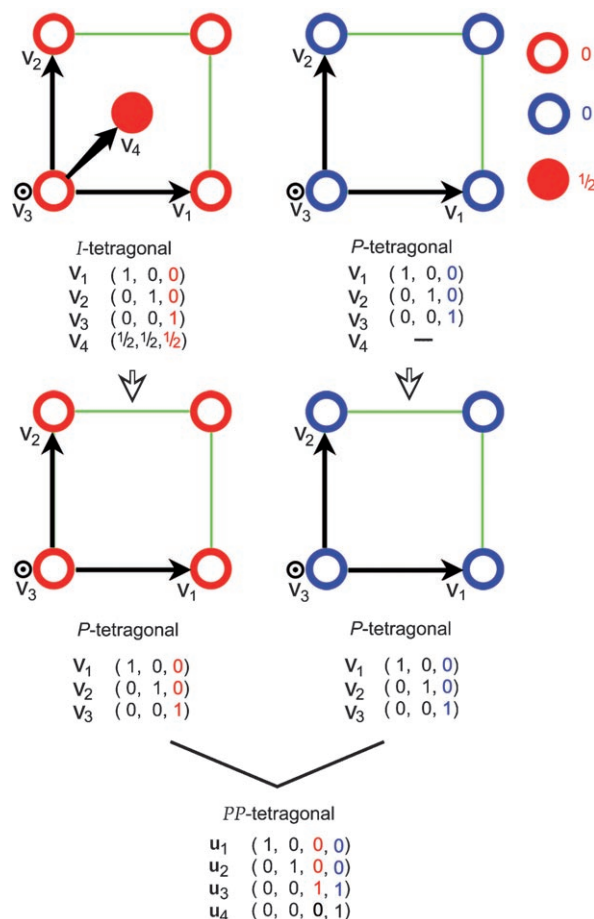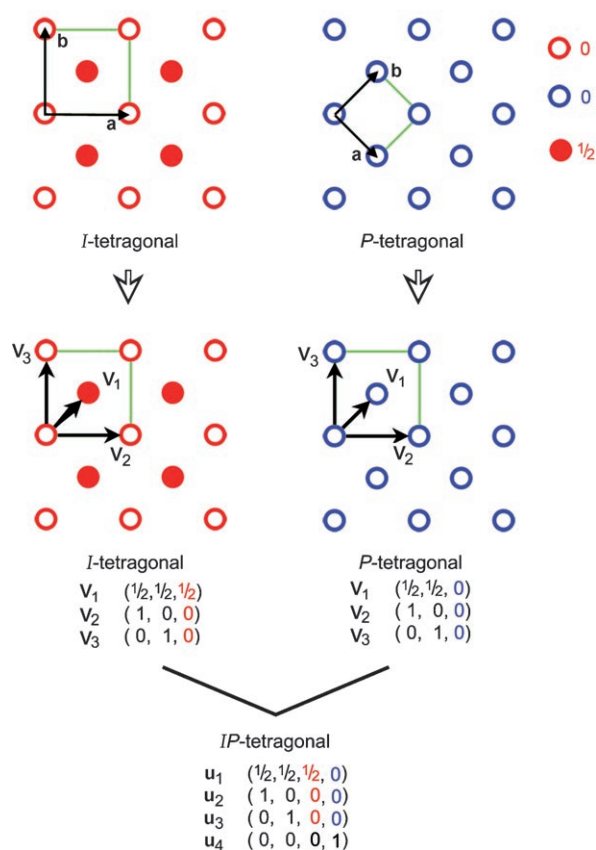


Figure 18. (3+1)D Bravais lattice generated from two 3D average substructures with *I*- and *P*-tetragonal Bravais lattice symmetry (the *a* and *b* axes are the common axes of the two average substructures). Top: 3D Bravais lattice vectors for the two 3D average substructures (some of these 3D vectors have no complementary vector in the other substructure, e.g., $\mathbf{v}_4$). By fusing the two sets of complementary 3D Bravais lattice vectors and adding the vector (0, 0, 0, 1) (middle and bottom), a (3+1)D *PP*-tetragonal Bravais lattice is obtained (bottom).

there are other rotations besides 45° that lead to coincident Bravais lattices, in no other case does such a rotation lead to two Bravais lattices that are fully complementary with one another. The restricted Bravais lattices based on these other rotations prove to be just one of the (3+1)D tetragonal Bravais lattices previously specified: *PP*, *II*, *IP*, and *PI*.[13] We have therefore successfully enumerated all (3+1)D tetragonal Bravais lattices.

### 7.4. (3+1)D Bravais Lattices by Bravais Class

The remaining Bravais classes can be treated in a similar manner. In this, our task is significantly simplified by two factors. First, we are only interested in (3+1)D symmetry

[13] These four cases simplify to just three in the Appendix.

Figure 19. (3+1)D Bravais lattice generated from two 3D substructures with *I*- and *P*-tetragonal Bravais lattice symmetry (the *a* and *b* axes are rotated by 45° with respect to each other). Top: two 3D Bravais lattices. Middle: two sets of 3D Bravais lattice vectors, all of which are complementary. The corresponding 3D Bravais lattice vectors are fused into the (3+1)D vectors. The vector (0, 0, 0, 1) is added to obtain a (3+1)D *IP*-tetragonal Bravais lattice. (compare Figure 18).

Figure 20. (3+1)D Bravais lattice generated from two 3D substructures with *P*- and *I*-tetragonal Bravais lattice symmetry (the *a* and *b* axes are rotated by 45° with respect to each other). Middle: the complementary 3D Bravais lattice vectors. By fusing the complementary 3D Bravais lattice vectors and adding the vector (0, 0, 0, 1), a (3+1)D *PI*-tetragonal Bravais lattice is obtained (compare Figures 16–19).

operations that are based on complementary 3D symmetry operations. In other words, for any composite crystal, the symmetry operations considered from each 3D substructure must contain the same point-group operations (with the same common-axis coefficients); therefore, the two substructures must share the same fixed 3D point group and the same rotation axes. It is for this reason that both substructures of (3+1)D tetragonal systems are always of tetragonal symmetry.

Second, we restrict our attention herein to (3+1)D systems. Each 3D substructure can therefore only have a single axis that is incommensurate with the axes of the other substructure. Thus, in the case of the tetragonal systems previously discussed, the only incommensurate axis must be the *c* axis (were the incommensurate axis either the *a* or *b* axis, the tetragonal-based equality of the *a* and *b* axes would essentially lead to two incommensurate axes).

We see how these restrictions play out in (3+1)D Bravais lattices for each of the individual Bravais classes below. We proceed from highest to lowest symmetry, from cubic to
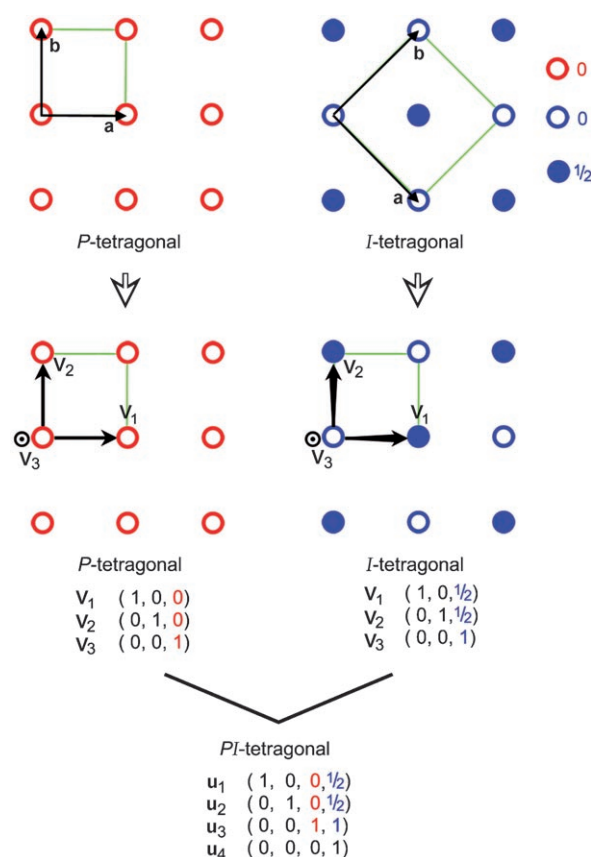
monoclinic.[14] The case of cubic symmetry can be quickly disposed of. Because both substructures must have the same point group, in this case both substructures would be of cubic symmetry. As $a = b = c$ in cubic systems, by symmetry it is not possible for the two substructures to differ with respect to a single axis. It is therefore impossible to create a (3+1)D cubic Bravais lattice.

Hexagonal/trigonal systems resemble more closely the case of tetragonal systems. For these Bravais lattices, there are two 3D Bravais classes, which we call *P*-hexagonal and *R*-hexagonal. For a (3+1)D system with a single set of incommensurate axes, only the unique *c* axis can function as the incommensurate axis (as in the tetragonal systems discussed above, were *a* or *b* the incommensurate axis, the sym-

---

[14] Herein, we restrict our attention to sets of substructure axes that are oriented along the same directions of the crystal. Thus, triclinic and monoclinic crystals, in which the incommensurate axes are not the monoclinic unique axis, will not be considered. In our opinion, these cases, which present their own novel complications in real space, are treated more appropriately within the context of (2+2) and (3+2)D crystals. Furthermore, they are of small practical importance when discussing intermetallic structures that tend to be dominated by higher-symmetry systems.

metry-induced equality of *a* and *b* would create a second incommensurate axis).

For the case whereby the common *a* and *b* axes are the same for both hexagonal/trigonal substructures, there are four possible (3+1)D combinations that must be considered: *PP*, *RR*, *RP*, and *PR*. Complementarity further limits the number of possibilities. Whereas the first two combinations lead to fully complementary Bravais lattices, the second two reduce in both cases to just *PP*-hexagonal symmetry. (The argument for this latter point, being in all respects identical to that used in Figure 18 for tetragonal systems, is not reproduced here.)

Just as with tetragonal symmetry, two cases whereby the two hexagonal cells are rotated with respect to each other must now be considered. In the first case, the second substructure is rotated by 30° with respect to the first, and $\mathbf{a}_2 = \frac{2}{3}\mathbf{a}_1 + \frac{1}{3}\mathbf{b}_1$ and $\mathbf{b}_2 = -\frac{1}{3}\mathbf{a}_1 + \frac{1}{3}\mathbf{b}_1$. The first substructure is *R*-hexagonal, and the second is *P*-hexagonal. As Figure 21 shows, the resultant (3+1)D Bravais lattice is *RP*-hexagonal.
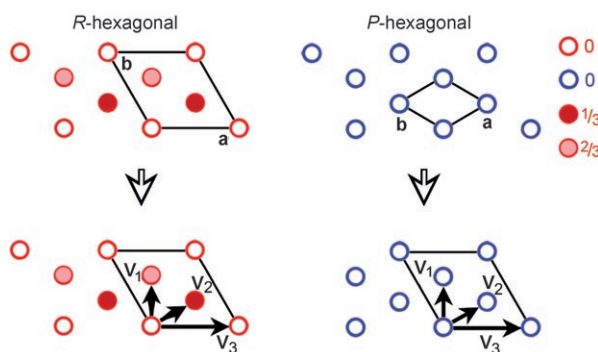


Figure 21. Complementary 3D vectors for two 3D substructures that have *R*- and *P*-hexagonal Bravais lattices symmetries (the *a* and *b* axes are rotated by 30° with respect to each other). Top: the two 3D Bravais lattices. Bottom: the two sets of complementary Bravais lattice vectors ($\mathbf{v}_1$, $\mathbf{v}_2$, and $\mathbf{v}_3$).

A second possibility is shown in Figure 22. The second substructure is again rotated by 30° with respect to the first, but now $\mathbf{a}_2 = \mathbf{a}_1 - \mathbf{b}_1$ and $\mathbf{b}_2 = \mathbf{a}_1 + 2\mathbf{b}_1$. Here the first and second substructures are *P*- and *R*-hexagonal, respectively; the resultant (3+1)D structure is *PR*-hexagonal. (Comparison of Figures 21 and 22 shows that these two cases are similar except that the roles of the first and second substructure are reversed.) This completes our enumeration of (3+1)D hexagonal/trigonal crystals.

The procedure for obtaining orthorhombic (3+1)D Bravais lattices is in some sense simpler than those discussed above. With orthorhombic symmetry, the *a*, *b*, and *c* axes are always rotoreflection axes and are the only such axes in the crystal. Complementarity of symmetry operations requires, therefore, that the cell axes for both substructures point along the same direction. As a consequence, unlike the previous cases, we need not consider rotations of any of the common axes. For (3+1)D orthorhombic systems, the *c* axis is conventionally the incommensurate axis.
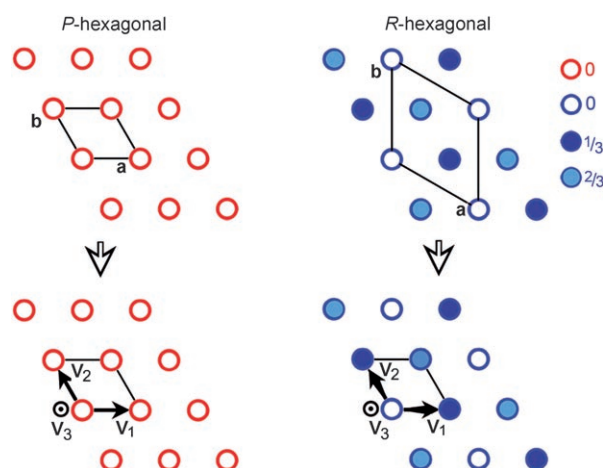


Figure 22. Complementary 3D vectors for two 3D substructures that have *P*- and *R*-hexagonal Bravais lattices symmetries (the *a* and *b* axes are rotated by 30° with respect to each other). Top: the two 3D Bravais lattices. Bottom: the two sets of complementary Bravais lattice vectors ($\mathbf{v}_1$, $\mathbf{v}_2$, and $\mathbf{v}_3$).

There are six 3D orthorhombic Bravais lattices in total: *P*, *A*, *B*, *C*, *I*, and *F*. We consider first the *C*- and *I*-orthorhombic systems (Figure 23). As discussed previously, the *C* and *I* lattices are fully complementary with each other and, when placed together, generate a (3+1)D *CI*- or *IC*-orthorhombic Bravais lattice.[15]
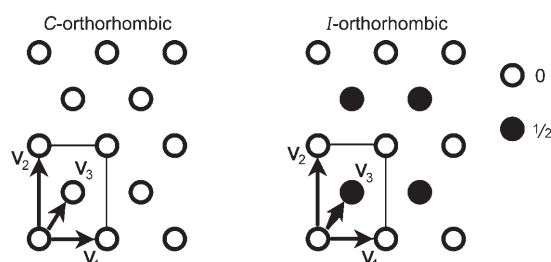


Figure 23. Complementary 3D vectors in *C*- and *I*-centered orthorhombic 3D Bravais lattices. Both lattices have a set of generating 3D Bravais lattice vectors ($\mathbf{v}_1$, $\mathbf{v}_2$, and $\mathbf{v}_3$).

In the same manner, we examine the *P*, *A*, *B*, and *F* lattices. As shown in Figure 24, any pair of these lattices can be fully complementary with each other, but only if some of the cell-axis lengths are halved or doubled with respect to each other. Thus, any pair of these four Bravais lattices can be combined to make a (3+1)D Bravais lattice.

Examination of Figures 23 and 24 shows, by contrast, that it is not possible to make fully complementary pairs of 3D Bravais lattices from a single 3D Bravais lattice from Figure 23 (*C* or *I*) and a single 3D Bravais lattice from Figure 24 (*P*, *A*, *B*, or *F*). Thus, any such pair would necessa-

[15] The order as to which substructure is designated the first and which the second determines which of the two possible (3+1)D Bravais lattices, *CI*- or *IC*-orthorhombic, is correct.
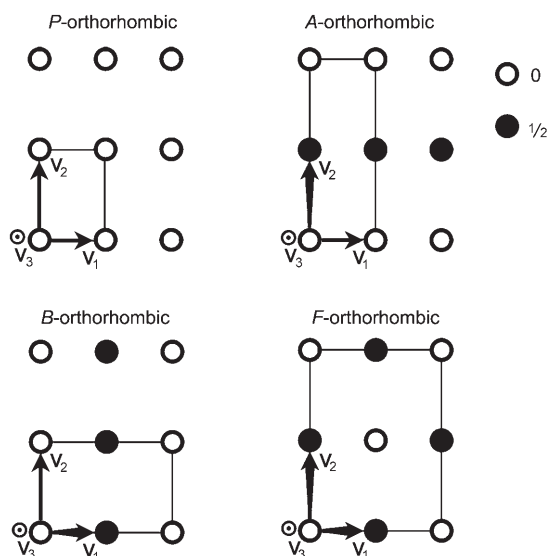
Figure 24. Complementary 3D vectors in *P*-, *A*-, *B*-, and *F*-centered orthorhombic 3D Bravais lattices. Each of these lattices has a set of generating 3D Bravais lattice vectors ($\mathbf{v}_1$, $\mathbf{v}_2$, and $\mathbf{v}_3$), all of which are complementary.

rily reduce to a pair of restricted Bravais lattices that are fully complementary to one another. These pairs of restricted Bravais lattices have been previously described.

We can now enumerate the number of possible (3+1)D orthorhombic crystals. For the two 3D orthorhombic Bravais classes, we can either choose any two Bravais classes from the two in Figure 23 (*C* or *I*) or two Bravais classes from the four in Figure 24 (*P*, *A*, *B*, or *F*). There are therefore 20 orthorhombic (3+1)D Bravais lattices in total ($20 = 2 \times 2 + 4 \times 4$).

We end this section with a discussion (3+1)D Bravais monoclinic systems, in which the incommensurate axis is the unique axis of the structure. It is conventional to choose the *c* axis as the unique axis. We restrict our attention to the *P*, *A*, and *B* lattices.[16] As Figure 25 shows, these three Bravais classes are fully complementary with one another. There are therefore nine (3+1)D monoclinic Bravais classes.
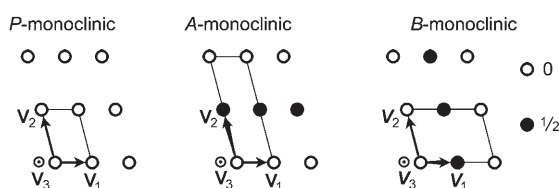


Figure 25. Complementary 3D vectors in *P*-, *A*-, and *B*-centered monoclinic 3D Bravais lattices (compare Figure 24).

[16] Both *A*- and *B*-centering have to be considered, as we have a fixed set of common axes. It is therefore possible that, with respect to the fixed set of common axes, the first substructure has *B*-centering but the second has *A*-centering.

It would be nice if we could say that we have fully enumerated all (3+1)D Bravais lattices or that we have given the (3+1)D Bravais lattice names that conform to the International Tables Volume C. Unfortunately, neither claim would be true. The nomenclature developed so far is quite different from that of the International Tables. Furthermore, we have not yet considered transformations of the cell axes, which may convert some of the enumerated Bravais classes into others. These points are considered in detail in the remaining sections.

We can, however, give some hint of the conclusions of the following sections. Table 5 gives the (3+1)D Bravais classes enumerated above, together with their names as found in the International Tables Volume C and Bravais lattice number. The (3+1)D cell-axis transformations that convert the enumerated Bravais classes into their canonically accepted form are also included.

### 7.5. Conventional Nomenclature for the (3+1)D Bravais Lattice

In the previous section, we derived an accurate nomenclature for the (3+1)D Bravais lattice, but unfortunately this nomenclature is not that of the International Tables Volume C. In this section, we present a procedure for converting the (3+1)D Bravais lattice names developed so far into the conventional format.

As Table 4 shows, the conventional designation of the (3+1)D Bravais lattice consists of a single 3D Bravais lattice symbol (i.e., *P*, *I*, *F*, etc.) followed by a three-dimensional vector (e.g., *PF*-orthorhombic is expressed as $P(\frac{1}{2}\frac{1}{2}\gamma)$, *IP*-tetragonal is designated $I(00\gamma)$). An examination of Table 4 shows the source of part of the name from the International Tables: the letter at the beginning of the name from the International Tables is the Bravais lattice type of the first substructure. The vector designation is more puzzling.

The reason why the vector portion of the name from the International Tables is so puzzling is that it is in fact a reciprocal lattice vector, the *q* vector often referred to in articles of higher-dimensional crystallography.[17,19][17] It is therefore quite difficult to associate a physical meaning with the *q*

[17] The *q* vector is defined in the following manner. The reciprocal basic vectors of the first substructure are designated $a^*$, $b^*$, and $c_1^*$. These three vectors form a reciprocal lattice. Some of the reflections can be indexed with integers based on these three vectors: they are called the main reflections. But in a (3+1)D crystal, there are additional reflections that are not describable in terms of these three vectors: they are called satellites. To index these satellites, one more reciprocal vector is needed: the *q* vector. With these four reciprocal vectors, one can then index all reflections with four integer indices as *hklm*. The selected *q* vector must fulfil the condition that if the main reflection is systematically absent, so are its satellites (*hkl*0 is the main reflection and *hklm* ($m \neq 0$) are its satellites). Although it is difficult to see the connection between the *q* vector thus defined and the real-space representation presented herein, we have verified for all relevant crystal systems that the real-space procedure given herein produces a satisfactory reciprocal-space *q* vector.

Table 4. (3+1)D Bravais lattices.

| Nomenclature herein | Bravais lattice type | | Bravais lattice no. | Cell-axis transformation[a] |
| | Int. Tables notation, untransformed cell axes | Int. Tables notation, transformed cell axes | | |
| --- | --- | --- | --- | --- |
| Monoclinic[b,c] | | | | |
| PP | $P(00\gamma)$ | $P(00\gamma)$ | 5 | |
| PA | $P(0\frac{1}{2}\gamma)$ | $P(0\frac{1}{2}\gamma)$ | 6 | |
| PB | $P(\frac{1}{2}0\gamma)$ | $P(\frac{1}{2}0\gamma)$ | 6 | |
| AP | $A(00\gamma)$ | $A(00\gamma)$ | 7 | |
| AA | $A(01\gamma)$ | $A(00\gamma)$ | 7 | $x_3' = x_3 + x_4$ |
| AB | $A(\frac{1}{2}0\gamma)$ | $A(\frac{1}{2}0\gamma)$ | 8 | |
| BP | $B(00\gamma)$ | $B(00\gamma)$ | 7 | |
| BA | $B(0\frac{1}{2}\gamma)$ | $B(0\frac{1}{2}\gamma)$ | 8 | |
| BB | $B(10\gamma)$ | $B(00\gamma)$ | 7 | $x_3' = x_3 + x_4$ |
| Orthorhombic[b] | | | | |
| PP | $P(00\gamma)$ | $P(00\gamma)$ | 9 | |
| PA | $P(0\frac{1}{2}\gamma)$ | $P(0\frac{1}{2}\gamma)$ | 10 | |
| PB | $P(\frac{1}{2}0\gamma)$ | $P(\frac{1}{2}0\gamma)$ | 10 | |
| PF | $P(\frac{1}{2}\frac{1}{2}\gamma)$ | $P(\frac{1}{2}\frac{1}{2}\gamma)$ | 11 | |
| AP | $A(00\gamma)$ | $A(00\gamma)$ | 15 | |
| AA | $A(01\gamma)$ | $A(00\gamma)$ | 15 | $x_3' = x_3 + x_4$ |
| AB | $A(\frac{1}{2}0\gamma)$ | $A(\frac{1}{2}0\gamma)$ | 16 | |
| AF | $A(\frac{1}{2}1\gamma)$ | $A(\frac{1}{2}0\gamma)$ | 16 | $x_3' = x_3 + x_4$ |
| BP | $B(00\gamma)$ | $B(00\gamma)$ | 15 | |
| BA | $B(0\frac{1}{2}\gamma)$ | $B(0\frac{1}{2}\gamma)$ | 16 | |
| BB | $B(10\gamma)$ | $B(00\gamma)$ | 15 | $x_3' = x_3 + x_4$ |
| BF | $B(1\frac{1}{2}\gamma)$ | $B(0\frac{1}{2}\gamma)$ | 16 | $x_3' = x_3 + x_4$ |
| FP | $F(00\gamma)$ | $F(00\gamma)$ | 17 | |
| FA | $F(01\gamma)$ | $F(01\gamma)$ | 18 | |
| FB | $F(10\gamma)$ | $F(10\gamma)$ | 18 | |
| FF | $F(11\gamma)$ | $F(00\gamma)$ | 17 | $x_3' = x_3 + x_4$ |
| IC | $I(00\gamma)$ | $I(00\gamma)$ | 12 | |
| II | $I(10\gamma)$ | $I(00\gamma)$ | 12 | $x_3' = x_3 + x_4$ |
| CC | $C(00\gamma)$ | $C(00\gamma)$ | 13 | |
| CI | $C(10\gamma)$ | $C(10\gamma)$ | 14 | |
| Tetragonal | | | | |
| PP | $P(00\gamma)$ | $P(00\gamma)$ | 19 | |
| PI | $P(\frac{1}{2}\frac{1}{2}\gamma)$ | $P(\frac{1}{2}\frac{1}{2}\gamma)$ | 20 | |
| IP | $I(00\gamma)$ | $I(00\gamma)$ | 21 | |
| II | $I(10\gamma)$ | $I(00\gamma)$ | 21 | $x_3' = x_3 + x_4$ |
| Hexagonal | | | | |
| RP | $R(00\gamma)$ | $R(00\gamma)$ | 22 | |
| $R_oR_o$ | $R_o(10\gamma)$[d] | $R_o(00\gamma)$ | 22 | $x_3' = x_3 + x_4$ |
| $R_oR_r$ | $R_o(01\gamma)$[d] | $R_o(00\gamma)$ | 22 | $x_3' = x_3 - x_4$ |
| PR | $P(\frac{1}{3}\frac{1}{3}\gamma)$ | $P(\frac{1}{3}\frac{1}{3}\gamma)$ | 23 | |
| PP | $P(00\gamma)$ | $P(00\gamma)$ | 24 | |

[a] If $x_j'$ is not listed, $x_j' = x_j$. [b] Through cell-axis transformation, some (3+1)D Bravais lattices can be converted into each other; see the Appendix. [c] Only cases whereby the unique axes of the monoclinic cells are incommensurate are considered here. [d] For rhombohedral lattices, $o$ stands for obverse, $r$ for reverse. By using the procedure defined in the text, the (3+1)D Bravais lattice $R(21\gamma)$ for the $R_oR_o$ system is obtained. From the reciprocal lattice definition of the $q$ vector, $(21\gamma)$ is the reciprocal vector between the main reflection, say, 000, and its first-order satellite reflection, say, $21\gamma$. We can, however, equivalently set another main reflection, say, 110, as the main reflection while retaining the same first-order satellite, $21\gamma$. With this change of main reflection, the vector between the main reflection and the first-order satellite becomes $21\gamma - 110 = 10\gamma$. Thus, $R(21\gamma)$ is equivalent to $R(10\gamma)$. Similarly for the $R_oR_r$ (3+1)D system, $R(10\gamma)$ becomes $R(01\gamma)$.

vector in direct space. However, such a physical meaning is given below.

The three components of the **q** vector ($q_1$, $q_2$, and $q_3$) are two simple numbers (0, 1, $\frac{1}{2}$ or $\frac{1}{3}$) followed by a third component, $\gamma$. In direct space, each of these three components can be taken as ratios. As noted previously, $\gamma$ is the ratio $c_1/c_2$ ($c_1$ and $c_2$ are the incommensurate axes in the two substructures). It would be nice if the first two numbers were similarly the ratios $a_1/a_2$ and $b_1/b_2$, but given that $a$ and $b$ are the commensurate axes and generally $a_1 = a_2$ and $b_1 = b_2$, it is clear that this definition would not be appropriate.

Instead, $q_1$ is the ratio of the $c$ and $a$ components of one of the three 3D generating vectors of the second substructure. Similarly, $q_2$ is the ratio of $c$ and $b$ of the second of the three 3D generating vectors. The crux of the difficulty in the determination of **q** is in deciding which of the three generating vectors of the second substructure should be the first and the second.

We illustrate the selection process with two examples. We consider first the *PF*-orthorhombic case, which is more properly called $P(\frac{1}{2}\frac{1}{2}\gamma)$ (Table 4). Figure 26 shows the three generating vectors of the second substructure in the *PF*-orthorhombic system. We now need a procedure that designates which of the **v** vectors should be used to generate $q_1$ and $q_2$, respectively.[18]

The first generating vector is chosen in a three-step process. First, we consider the subset of all the Bravais lattice points of the second substructure in Figure 26 that has the smallest positive (nonzero) value in the $a$ direction, then we choose among this subset the Bravais lattice points that have the smallest nonnegative value in the $b$ direction. Finally, among this further subset, we select the Bravais lattice vector that has the smallest nonnegative coefficient in the $c$ direction. The second generating vector is chosen by a similar process, but the smallest coefficient in the $b$ direction is selected first, followed by a narrowing of choice with respect to the $a$ axis, and finally a further narrowing with respect to the $c$ axis.

By following this procedure, $\mathbf{v}_1$, $(1,0,\frac{1}{2})$, is determined as the first generating vector. Given that $q_1$ is the value of the $c$ coordinate divided by the $a$ coordinate, we find that $q_1 = \frac{1}{2}$, whereby $\frac{1}{2} = \frac{1}{2} \div 1$. Similarly,
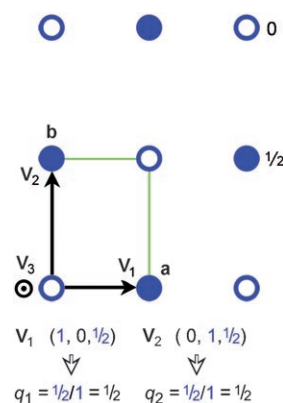


Figure 26. $q_1$ and $q_2$ for the (3+1)D *PF*-orthorhombic system. $q_1$ and $q_2$ are determined by the 3D *F*-centered part of the *PF*-orthorhombic system. This figure shows a 3D *F*-centered Bravais lattice. For $q_1$, we select the vector $\mathbf{v}_1$, which is the Bravais lattice vector with the smallest positive value along the $a$ direction and the smallest nonnegative value along the $b$ and $c$ directions. For $q_2$, we select $\mathbf{v}_2$, which is the Bravais lattice vector with the smallest positive value along the $b$ direction and the smallest nonnegative value along the $a$ and $c$ directions. $q_1$ and $q_2$ are obtained from the equations shown in the figure.

---

18 We need only select among the 3D generating vectors of the second substructure. Full information about the generating vectors of the first substructure is already contained in the $P$ portion of the name $P(\frac{1}{2}\frac{1}{2}\gamma)$.
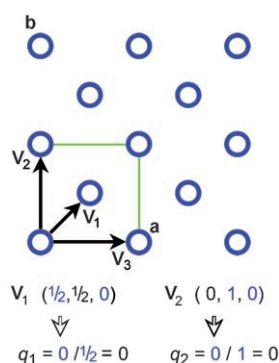
Figure 27. $q_1$ and $q_2$ for the (3+1)D *IP*-tetragonal system. $q_1$ and $q_2$ are determined by the 3D *P*-lattice part of the *IP*-tetragonal system. This figure shows such a 3D *P*-tetragonal Bravais lattice. As with Figure 26, the vector $\mathbf{v}_1$ is the Bravais lattice with the smallest positive value along the *a* direction and the smallest nonnegative value along the *b* and *c* directions. However, the vector with the smallest positive value along the *b* direction and the smallest nonnegative value along the *a* and *c* directions is again $\mathbf{v}_1$. We therefore choose the vector $\mathbf{v}_2$ as the Bravais lattice vector with the second-smallest nonnegative value along the *b* direction and the smallest value along the *a* and *c* directions. $q_1$ and $q_2$ are obtained from $\mathbf{v}_1$ and $\mathbf{v}_2$ from the equations shown in the figure.

the second generating vector is found to be $\mathbf{v}_2$, (0, 1, $^1\!/_2$), and (given that $q_2$ is the value of the *c* coordinate divided by the *b* coordinate) $q_2 = ^1\!/_2$, whereby $^1\!/_2 = ^1\!/_2 \div 1$. We conclude that the $\mathbf{q}$ vector is ($^1\!/_2 ^1\!/_2 \gamma$), and the conventional (3+1)D Bravais lattice symbol is $P(^1\!/_2 ^1\!/_2 \gamma)$.

The second example illustrates a pitfall in the procedure. This example is based on the *IP*-tetragonal lattice, which was previously derived for Nowotny chimney–ladder phases (Figures 17 and 27). The first chosen generating vector is the Bravais lattice vector with the smallest *a*-axis coordinate, followed by the smallest *b*-axis coordinate, and finally the smallest *c*-axis coordinate. This vector is $\mathbf{v}_1$, ($^1\!/_2$, $^1\!/_2$, 0), and so $q_1 = 0$, whereby $0 = 0 \div ^1\!/_2$.

The pitfall arises with the second chosen generating vector. Our procedure for choosing this vector (i.e., choosing the vector with the smallest *b* coefficient, followed by the smallest *a* coefficient, and finally the smallest *c* coefficient) leads to the same generating vector as the one initially chosen, $\mathbf{v}_1$, ($^1\!/_2$, $^1\!/_2$, 0).

The second chosen generating vector must be different from the first. We therefore adopt an alternative procedure. For the second chosen vector, we consider instead generating vectors with the second-smallest positive value along the *b* direction, followed by the smallest coefficients in the *a* and *c* directions. By this procedure, the second chosen generating lattice vector is (0,1,0), or $\mathbf{v}_2$ in Figure 27. We deduce that $q_2 = 0$, whereby $0 = 0 \div ^1\!/_2$. The $\mathbf{q}$ vector is therefore $(00\gamma)$, and the Bravais lattice type is $I(00\gamma)$.

We are now in a position to state unambiguously the full conventional (3+1)D space group. We combine the (3+1)D Bravais lattice with the previously derived 4D rotoreflection symbols. For Nowotny chimney–ladder phases, the Bravais lattice is $I(00\gamma)$, whereas the previously derived rotoreflection symbol is $4_1/amd\ 00ss$; the complete space-group name is, therefore, $I4_1/amd(00\gamma)00ss$.[7–10]

## 8. Conclusions

Although this is a long article, we hope that it conveys the simple message that higher-dimensional crystallography is just a continuation of ordinary 3D crystallogaphy. Crystallographers who are willing to accept new twists to traditional concepts should be able to apply higher-dimensional crystallography in their work. Furthermore, there are substantial advantages of higher-dimensional descriptions for many complex 3D crystal structures. $Mn_{27}Si_{47}$[54] has 296 atoms in its 3D crystal unit cell, but in 4D it has just two crystallographically inequivalent atoms (one manganese and one silicon atom). Rb-IV,[25,26] which is incommensurate (and so not even a crystal in 3D), also has just two crystallographically inequivalent atoms in its 4D unit cell.

These substantial reductions are also found for numerous other structures. We conclude this Focus Review by tabulating some of these systems. We restrict our attention to structures reported in Pearson's Tables of Intermetallic Compounds[24] and to elemental structures under pressure. Tables 5 and 6 list those compounds that can be appropriately termed composite structures. As these tables show, composite structures are found in borides, gallides, germanides, stannides, antimonides, sulfides, and other intermetallic formulations.

As the methods of space-group determination given herein are straightforward, these tables also list the appropriate 4D space group of each of these composite systems. In some cases, the 4D space group listed differs from the one initially reported. In other cases, the 4D space group is listed where not specified by the original authors. We hope that these examples will help illustrate the versatility of determining 4D space groups from real 3D crystal structures.

As stated repeatedly, the ease by which the (3+1)D space group can be deduced resides in the fact that we only need to search for two separate 3D space groups, one for each of the 3D components of the composite structure. Furthermore, owing to the principle of complementarity, only those separable 3D operations that have common compo-

Table 5. Composite high-pressure elemental structures.[a]

| Formula | Superspace group | No. | No. of atoms | Reference |
|---|---|---|---|---|
| K-III | $I4/mcm(00\gamma)$ | 140.1 | 2 | [77,78] |
| Rb-IV | $I4/mcm(10\gamma)s000$[b] | 140.2 | 2 | [25,26,77] |
| Sr-V | $I4/mcm(00\gamma)$ | 140.1 | 2 | [77,79] |
| Ba-IVa | $I4/mcm(00\gamma)+$ | 140.1 | 2 | [77,80] |
|  | $B2/b(\alpha\beta1)$ | 15.1 | 2 |  |
| Ba-IVb | $I4/mcm(00\gamma)+$orthorhombic | 140.1 | 2 | [77,80] |
| Ba-IVc | unknown |  |  | [77,80] |
| Sc-II | $I4/mcm(00\gamma)$ | 140.1 | 2 | [28] |
| As-III | $B2/b(\alpha\beta1)$ | 15.1 | 2 | [77,81] |
| Sb-II | $I4/mcm(10\gamma)000s$ | 140.3 | 2 | [77,82,83] |
| Sb-IV | $B2/b(\alpha\beta1)$ | 15.1 | 2 | [77,81] |
| Bi-III | $I4/mcm(10\gamma)000s$ | 140.3 | 2 | [77,82,83] |

[a] Owing to the methodology of this article, all $W_2$ matrices that have the *c* axis as the incommensurate axis have the simplest form (1 0 0 0, 0 1 0 0, 0 0 0 1, 0 0 1 0). [b] Reference [77] gives Rb-IV to be $I'4/mcm(00\gamma)000s$.

Table 6. Known composite intermetallic compounds.[a]

| Formula | Superspace group | No. | No. of atoms | Reference |
|---|---|---|---|---|
| $LiB_x$ | $P\bar{1}(\alpha\beta\gamma)$ | 2.1 | 3 | [6] |
| $(LaS)_{1.196}VS_2$ | $P\bar{1}(\alpha\beta\gamma)$ | 2.1 | 4 | [3] |
| $(EuS)_{1.173}NbS_2$ | $F2mm(11\gamma)$ | 42.7 | 4 | [84] |
| $La_8Nb_7S_{22}$ | $F2mm(10\gamma)0s0$ | 42.10 | 4 | [85–87] |
| $Na_9Sn_4$ | $Cmcm(00\gamma)$ | 63.1 | 2 | [88] |
| $Ca_{28}Ga_{11}$ | $Cmcm(10\gamma)$ | 63.3 | 2 | [89] |
| $Ru_{25}Y_{44}$ | $Abma(01\gamma)ss0$ | 64.7 | 6 | [90] |
| $Pt_7Zn_{12}$ | $Ammm(01\gamma)0s0$ | 65.10 | 2 | [30] |
| $Ca_7Rh_{20}B_{14}$ | $Fmmm(00\gamma)$ | 69.1 | 3 | [65] |
| $Sr_5Rh_{14}B_{10}$ | $Fmmm(00\gamma)$ | 69.1 | 3 | [65] |
| $Ba_6Hf_5S_{16}$ | $Fmmm(00\gamma)$ | 69.1 | 3 | [91] |
| $Ba_5Hf_4S_{13}$ | $Fmmm(00\gamma)$ | 69.1 | 3 | [91] |
| $Ni_{16}Zn_{53}$ | $Fmmm(11\gamma)s00$ | 69.2 | 4 | [58,92,93] |
| $Ta_4P_4S_{29}$ | $P4_21 2(00\gamma)q00$ | 94.2 | 9 | [94] |
| $Gd_2Fe_7B_7$ | $P4_2/nmc(00\gamma)s0s0$ | 137.2 | 3 | [57] |
| $Nd_5Fe_{18}B_{18}$ | $P4_2/nmc(00\gamma)s0s0$ | 137.2 | 3 | [57,95,96] |
| $Sm_{17}Fe_{60}B_{60}$ | $P4_2/nmc(00\gamma)s0s0$ | 137.2 | 3 | [97] |
| $Ho_5Fe_{17}B_{17}$ | $P4_2/nmc(00\gamma)s0s0$ | 137.2 | 3 | [98] |
| $Sm_{11}Co_{40}B_{40}$ | $P4_2/nmc(00\gamma)s0s0$ | 137.2 | 3 | [99] |
| $Nd_{19}Fe_{68}B_{68}$ | $P4_2/nmc(00\gamma)s0s0$ | 137.2 | 3 | [100] |
| $Pr_{41}Mn_{140}B_{140}$ | $P4_2/nmc(00\gamma)s0s0$ | 137.2 | 3 | [101] |
| $Pr_7Re_{24}B_{24}$ | $P4_2/ncm(00\gamma)s00s$ | 138.2 | 6 | [101] |
| $Ce_3Ga_{15}Ni_2$ | $I4/mmm(00\gamma)$ | 139.1 | 2 | [102] |
| $Ba_9Fe_{16}S_{32}$ | $I4/mmm(10\gamma)00ss$[b] | 139.3 | 3 | [32,33] |
| $Ba_5Fe_9S_{18}$ | $I4/mmm(10\gamma)00ss$[b] | 139.3 | 3 | [31,33] |
| $Rh_{10}Ga_{17}$ | $I4_1/amd(00\gamma)00ss$ | 141.2 | 2 | [29] |
| $Rh_{17}Ge_{22}$ | $I4_1/amd(00\gamma)00ss$ | 141.2 | 2 | [56] |
| $Mo_{13}Ge_{23}$ | $I4_1/amd(00\gamma)00ss$ | 141.2 | 2 | [55] |
| $V_{17}Ge_{31}$ | $I4_1/amd(00\gamma)00ss$ | 141.2 | 2 | [55] |
| $Mn_{11}Si_{19}$ | $I4_1/amd(00\gamma)00ss$ | 141.2 | 2 | [52] |
| $Mn_{15}Si_{26}$ | $I4_1/amd(00\gamma)00ss$ | 141.2 | 2 | [53] |
| $Mn_{27}Si_{47}$ | $I4_1/amd(00\gamma)00ss$ | 141.2 | 2 | [54] |
| $(Mo/Rh)Ge_x$ | $I4_1/amd(00\gamma)00ss$ | 141.2 | 2 | [8] |
| $(Cr/Mo)Ge_x$ | $I4_1/amd(00\gamma)00ss$ | 141.2 | 2 | [9] |
| $ZrBi_{1.62}$ | $I4_1/amd(00\gamma)00ss$ | 141.2 | 2 | [10] |
| $La_{1.18}Rh_3In_2$ | $R3m(00\gamma)$ | 160.1 | 3 | [14] |
| $Sr_xTiS_{2.84}$ | $R3m(00\gamma)0s$ | 160.2 | 3 | [59,103] |
| $Mn_{5.11}Ge_2$ | $P\bar{3}m1(00\gamma)0s$ | 164.2 | 7 | [104] |
| $Yb_8In_3$ | $R\bar{3}m(00\gamma)0s$ | 166.2 | 2 | [105] |
| $Pd_8Sb_3$ | $R\bar{3}m(00\gamma)0s$ | 166.2 | 2 | [106] |

[a] Owing to the methodology of this article, all $W_2$ matrices that have the $c$ axis as the incommensurate axis have the simplest form (1 0 0 0, 0 1 0 0, 0 0 0 1, 0 0 1 0). [b] Reference [32] gives the superspace group for these systems as $I4mm(10\gamma)0ss$, which is a subgroup of the group listed here.

nents along the common axes can be joined into higher-dimensional symmetry operations. The separability of the component parts and the complementarity of their joint symmetries lead to the facile application of higher-dimensional crystallography to everyday crystal systems.

# 9. Appendix

## 9.1. Canonical (3+1)D Bravais Lattices

We have discussed how a (3+1)D Bravais lattice can be fashioned from two fully complementary 3D Bravais lattices, and how these (3+1)D lattices are conventionally represented by a single 3D lattice designation followed by a $q$ vector. Thus, the (3+1)D Bravais lattices of Nowotny chim-

ney–ladder phases and Rb-IV were found to be $I(00\gamma)$ and $I(10\gamma)$, respectively. Table 4, however, shows that these two Bravais lattices can both be represented by the same symbol $I(00\gamma)$, and that there is a cell-axis transformation that converts one of the two (3+1)D Bravais lattices into the other.

The existence of such cell-axis transformations may not be surprising. For example, cell transformations exist that convert $F$- and $C$-centered tetragonal cells into $I$- and $P$-centered cells, respectively. In the sections below, we review the standard transformations of 3D Bravais lattice cell axes and illustrate how these transformations play out in (3+1) dimensions.

### 9.1.1. A Review of 3D Bravais Lattice Determination

In ordinary 3D crystallography, the unit cell is chosen with respect to the crystal symmetry. Thus, in tetragonal crystals, the $a$, $b$, and $c$ axes are conventionally orthogonal to one another, and $a=b$ but in general $a\neq c$. These axes are chosen so that they are aligned with the rotoreflections found in the crystal structure. Ultimately, it is the symmetries in the crystal and not the metrics of the cell axes that determine the symmetry of the Bravais lattice.

It is the requirement that the cell axes align themselves with many of the symmetry operations of the crystal that leads to nonprimitive unit cells. Familiar Bravais lattice designations such as $A$, $B$, $C$, $I$, and $F$ are due to the fact that cells larger than the primitive cell must be chosen to align cell axes with symmetry operations. Thus, in standard settings, we have $P$- and $C$-monoclinic cells, $P$-, $C$-, $I$-, and $F$-orthorhombic cells, and $P$- and $I$-tetragonal cells.

As the above list demonstrates, the number of standard Bravais lattice types varies depending on the crystal system. Those Bravais lattice types missing from a given crystal system are often absent because there exist cell-axis transformations that turn a given Bravais lattice into another standard Bravais lattice type.

We give a single example from 3D crystallography.[19] In standard settings, there are no $I$-centered monoclinic cells. The operative word here is standard, as $I$-centered monoclinic cells do exist. An example of one is shown in Figure 28; the $I$-centered cell is in green. However, an alternative choice is the $C$-centered cell (in black). The standard setting is the $C$-centered cell, not the $I$-centered cell.

Why are there no standard $I$-centered monoclinic cells but standard $I$-centered orthorhombic cells? The answer has to do with the nature of monoclinic symmetry, orthorhombic symmetry, and the cell-axis transformation implicit in Figure 28. This cell-axis transformation requires a change in the $a$ axis but none in the $b$ and $c$ axes. If we call the $C$- and $I$-centered $a$ axes $a_C$ and $a_I$, respectively, the following relation holds: $\mathbf{a}_C = \mathbf{a}_I + \mathbf{c}$. This cell-axis transformation conforms to the requirements of a conventional monoclinic cell (that the $b$ axis is unique, i.e., perpendicular to the other axes both before and after the cell transformation), but does not

---

[19] It turns out that this single example, in various guises, accounts for all but one of the (3+1)D transformations given in Table 4.
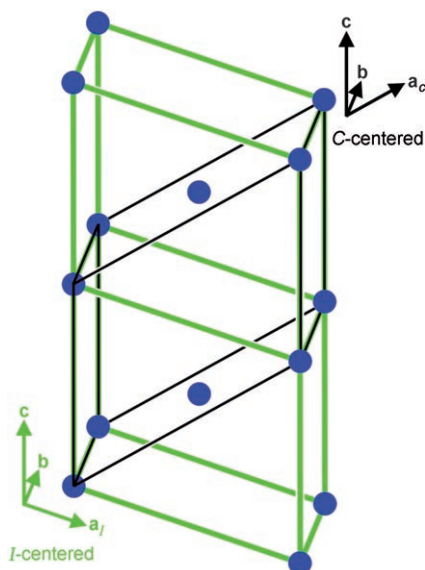
Figure 28. Relationship between the nonstandard 3D $I$-centered monoclinic cell and the standard 3D $C$-centered monoclinic cell. The $I$-centered cell is shown in green, the $C$-centered cell in black. Although both the $I$- and $C$-centered cells correspond to the same lattice, the unit cells are different. Cell-axis vectors for the $I$- and $C$-centered cells are shown in green and black, respectively.

fulfil the conditions of an orthorhombic cell, that the $a$ axis remains equally perpendicular to the other two axes. Thus (and this is important in the next sections), we consider only those cell-axis transformations that respect the symmetries of the crystal system.

## 9.2. (3+1)D Tetragonal Cell Axes

The short review given above illustrates that if we are to find allowed (3+1)D cell transformations, we need to specify the exact cell-axis requirements for any given (3+1)D Bravais crystal system: not the lattice generating vectors that have hitherto been our main concern, but rather the cell axes themselves. (A 3D example may be useful here to clarify this distinction. For a 3D $I$-centered tetragonal Bravais lattice, while the generating vectors can be taken as ($\frac{1}{2}$, $\frac{1}{2}$, $\frac{1}{2}$), (1, 0, 0), and (0, 1, 0), the cell-axis vectors correspond to the $a$, $b$, and $c$ directions.) Thus, we are not interested in the four generating vectors $\mathbf{u}_i$, but rather the (3+1)D vectors discussed at the beginning of this article, $\mathbf{x}_i$.

As an illustration, we consider the $\mathbf{x}_i$ vectors for a tetragonal system. In this system, the common axes are fairly straightforward. The common 3D $a$ and $b$ axes are perpendicular to each other, and $a=b$. Given that $\mathbf{x}_1 = \mathbf{a}$ and $\mathbf{x}_2 = \mathbf{b}$, $\mathbf{x}_1$ and $\mathbf{x}_2$ are perpendicular to each other, and $|\mathbf{x}_1| = |\mathbf{x}_2|$.

We turn now to the $\mathbf{x}_3$ and $\mathbf{x}_4$ axes. The latter is defined to be perpendicular to the real 3D physical space. It is therefore perpendicular to two of the real-space axes, $a$ and $b$ ($\mathbf{x}_4$ is of unit length). Similarly, $\mathbf{x}_3$ is perpendicular to the common axes $a$ and $b$, but is not perpendicular to the in-

commensurate $c$ axes.[20] As noted previously, the angle between these axes is $|\cot^{-1}(c_1/\gamma)|$; therefore, $\mathbf{x}_3$ and $\mathbf{x}_4$ are not perpendicular to each other. In summary, in a (3+1)D tetragonal cell, $\mathbf{x}_1$ and $\mathbf{x}_2$ are equal in magnitude and are perpendicular to each other, $\mathbf{x}_3$ and $\mathbf{x}_4$ are perpendicular to $\mathbf{x}_1$ and $\mathbf{x}_2$ but are not perpendicular to each other. Finally, $\mathbf{x}_4$ is of unit length. These are the metric requirements of a (3+1)D tetragonal cell.

Our interest here is in cell-axis transformations that preserve the $\mathbf{x}_i$ relationships specified above. One such transformation type, which will play a significant role in the next section, are cell-axis transformations that preserve the cell axes $\mathbf{x}_1$, $\mathbf{x}_2$, and $\mathbf{x}_4$, but for which there is a new cell axis $\mathbf{x}_3'$, which is a linear combination of $\mathbf{x}_3$ and $\mathbf{x}_4$. This cell-axis transformation maintains all the metric requirements of a (3+1)D tetragonal cell. Such transformations are therefore allowed in tetragonal symmetry.

### 9.2.1. An Example of a (3+1)D Cell Transformation for Rb-IV

We apply a cell transformation of the type specified in the previous section to the Rb-IV system. This system is $I$-tetragonal, and the first and second chosen Bravais lattice vectors are ($\frac{1}{2}$, $\frac{1}{2}$, $\frac{1}{2}$) and (0, 1, 0) (Figure 16). Given that $q_1$ is the ratio of the $c$- and $a$-axis coordinates for the first chosen vector and that $q_2$ is a similar ratio of the $c$ and $b$ axes for the second chosen vector, we find that $\mathbf{q}$ is (10$\gamma$), and the overall Bravais class is $I(10\gamma)$. We now seek a cell-axis transformation that converts this designation into the canonical one in the International Tables Volume C.

As mentioned above, for tetragonal systems any cell transformation in which $\mathbf{x}_1$, $\mathbf{x}_2$, and $\mathbf{x}_4$ are unchanged but where $\mathbf{x}_3'$ is a linear combination of $\mathbf{x}_3$ and $\mathbf{x}_4$ preserves the overall tetragonal nature of the (3+1)D Bravais lattice. We consider one such transformation: the one in which $\mathbf{x}_3' = \mathbf{x}_3 + \mathbf{x}_4$.

We need to calculate how such a cell-axis transformation changes the cell-axis coordinates. To do so, we can represent a vector with respect to either the old or the new basis vectors, but in either case the two representations are equal. Thus, if we take the coordinates of a given vector to be $\xi_i$ and $\xi_i'$ with respect to the two sets of cell axes, then $\Sigma\xi_i\mathbf{x}_i = \Sigma\xi_i'\mathbf{x}_i'$. Given the definitions of the $\mathbf{x}_i'$ vectors, $\xi_i = \xi_i'$ for $i = 1$, 2, or 3, and $\xi_4 = \xi_3' + \xi_4'$ (or equivalently, $\xi_4' = \xi_4 - \xi_3$).

Let us apply these coordinate transforms to the Rb-IV system. The left half of Figure 29 shows the generating vectors of the (3+1)D Bravais lattice of this structure. These four vectors are initially represented with respect to the old cell-axis vectors. We then transform the coordinates as described above. The new cell-axis representations, $\mathbf{u}_j$, are given in the bottom right of Figure 29.

Interestingly, this is not the first time in this article that we have come across this new set of $\mathbf{u}_j$ vectors. In fact, these are the same vectors previously encountered in Figure 19 for the $IP$-tetragonal ($IP$-tetragonal being $I(00\gamma)$ in the In-

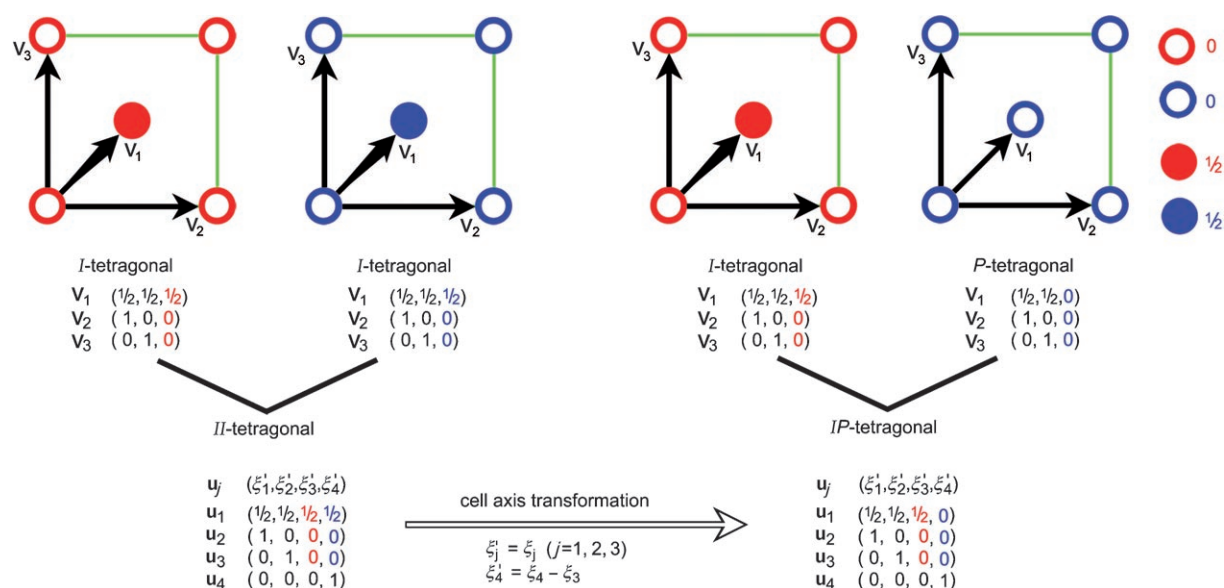[20] A review of $\mathbf{x}_i$ axes for (2+1)D systems may be helpful; see Figure 8.

Figure 29. Relationship between the nonstandard $(3+1)$D $II$-tetragonal Bravais lattice ($I(10\gamma)$) and the standard $(3+1)$D $IP$-tetragonal Bravais lattice ($I(00\gamma)$). Left: two 3D Bravais lattices (red and blue), both of which are $I$-centered and have complementary 3D Bravais vectors (middle). These two sets of 3D Bravais lattice vectors are fused to obtain a set of $(3+1)$D vectors with $(3+1)$D $II$-tetragonal Bravais lattice symmetry ($I(10\gamma)$). Right: two 3D Bravais lattices that are $I$-centered (red) and $P$-centered (blue). Their 3D Bravais vectors are shown below. By fusing these two sets of vectors, a set of $(3+1)$D vectors with $IP$-tetragonal Bravais lattice symmetry ($I(00\gamma)$) is obtained. The cell transformation that changes the cell-axis coordinates (bottom) converts the $(3+1)$D $II$-tetragonal symmetry ($I(10\gamma)$) on the left into the $(3+1)$D $IP$-tetragonal symmetry ($I(00\gamma)$) on the right.

ternational Tables) system. In other words, under the cell transformation described above, $II$-tetragonal ($I(10\gamma)$ of the International Tables) transforms into the $IP$-tetragonal (or $I(00\gamma)$) Bravais lattice. As this cell transformation respects the constraints of tetragonal symmetry, $II$-tetragonal and $IP$-tetragonal are equivalent Bravais lattices.

## Acknowledgements

[1] T. Hahn, *International Tables for Crystallography Vol. A: Space-Group Symmetry*, 5th ed., Kluwer Academic Publishers, Dordrecht, **2002**.
[2] M. Boström, S. Lidin, *J. Alloys Compd.* **2004**, *376*, 49.
[3] L. Cario, A. Meerschaut, B. Corraze, O. Chauvet, *Mater. Res. Bull.* **2005**, *40*, 125.
[4] M. Evain, V. Petricek, Y. Moëlo, C. Maurel, *Acta Crystallogr. Sect. B* **2006**, *62*, 775.
[5] L. Norén, R. L. Withers, F. J. Brink, *J. Solid State Chem.* **2005**, *178*, 2133.
[6] M. Wörle, R. Nesper, T. K. Chatterji, *Z. Anorg. Allg. Chem.* **2006**, *632*, 1737.
[7] A. Yamamoto, *Acta Crystallogr. Sect. A* **1993**, *49*, 831.
[8] F. E. Rohrer, H. Lind, L. Eriksson, A.-K. Larsson, S. Lidin, *Z. Kristallogr.* **2000**, *215*, 650.
[9] F. E. Rohrer, H. Lind, L. Eriksson, A.-K. Larsson, S. Lidin, *Z. Kristallogr.* **2001**, *216*, 190.
[10] M. Boström, H. Lind, S. Lidin, R. Niewa, Y. Grin, *Solid State Sci.* **2006**, *8*, 1173.
[11] J. Sun, G. Li, Z. Li, L. You, J. Lin, *Inorg. Chem.* **2006**, *45*, 8394.
[12] K. E. Stitzer, A. E. Abed, J. Darriet, H. C. zur Loye, *J. Am. Chem. Soc.* **2004**, *126*, 856.
[13] S. van Smaalen, A. Meetsma, G. A. Wiegers, J. L. de Boer, *Acta Crystallogr. Sect. B* **1991**, *47*, 314.
[14] S. Esmaeilzadeh, V. I. Zaremba, Y. M. Kalychak, R. D. Hoffmann, R. Pöttgen, *Solid State Sci.* **2002**, *4*, 93.
[15] A. Janner, T. Janssen, *Phys. Rev. B* **1977**, *15*, 643.
[16] P. M. de Wolff, T. Janssen, A. Janner, *Acta Crystallogr. Sect. A* **1981**, *37*, 625.
[17] A. Janner, T. Janssen, P. M. de Wolff, *Acta Crystallogr. Sect. A* **1983**, *39*, 658.
[18] A. Yamamoto, *Acta Crystallogr. Sect. A* **1992**, *48*, 476.
[19] S. van Smaalen, *Cryst. Rev.* **1995**, *4*, 79.
[20] I. Aramburu, G. Madariaga, J. M. Pérez-Mato, *J. Phys. Condens. Matter* **1995**, *7*, 6187.
[21] S. van Smaalen, *Z. Kristallogr.* **2004**, *219*, 681.
[22] P. M. de Wolff, *Acta Crystallogr. Sect. A* **1984**, *40*, 34.
[23] T. Janssen, A. Janner, A. Looijenga-Vos, P. M. de Wolff, *International Tables for Crystallography Vol. C, Section 9.8: Incommensurate and Commensurate Modulated Structures*, Kluwer Academic Publishers, Dordrecht, **1998**.
[24] P. Villars, L. D. Calvert, *Pearson's Handbook of Crystallographic Data for Intermetallic Phases*, 2nd ed., ASM International, Materials Park, **1991**.
[25] U. Schwarz, A. Grzechnik, K. Syassen, I. Loa, M. Hanfland, *Phys. Rev. Lett.* **1999**, *83*, 4085.
[26] M. I. McMahon, S. Rekhi, R. J. Nelmes, *Phys. Rev. Lett.* **2001**, *87*, 055501.
[27] H. Fujihisa, Y. Akahama, H. Kawamura, Y. Gotoh, H. Yamawaki, M. Sakashita, S. Takeya, K. Honda, *Phys. Rev. B* **2005**, *72*, 132103.
[28] M. I. McMahon, L. F. Lundegaard, C. Hejny, S. Falconi, R. J. Nelmes, *Phys. Rev. B* **2006**, *73*, 134102.
[29] H. Völlenkle, A. Wittmann, H. Nowotny, *Monatsh. Chem.* **1967**, *98*, 176.

[30] W. Carl, K. Schubert, *J. Less-Common Met.* **1969**, *19*, 279.

[31] I. E. Grey, *Acta Crystallogr. Sect. B* **1975**, *31*, 45.

[32] J. T. Hoggins, H. Steinfink, *Acta Crystallogr. Sect. B* **1977**, *33*, 673.

[33] M. Onoda, K. Kato, *Acta Crystallogr. Sect. B* **1991**, *47*, 630.

[34] D. Shechtman, I. Blech, D. Gratias, J. W. Cahn, *Phys. Rev. Lett.* **1984**, *53*, 1951.

[35] V. Elser, C. L. Henley, *Phys. Rev. Lett.* **1985**, *55*, 2883.

[36] W. Steurer, *Acta Crystallogr. Sect. B* **1989**, *45*, 534.

[37] A. Yamamoto, S. Weber, A. Sato, K. Kato, K. Ohshima, A. P. Tsai, A. Niikura, K. Hiraga, A. Inoue, T. Masumoto, *Philos. Mag. Lett.* **1996**, *73*, 247.

[38] H. Zhang, Z. B. He, P. Oleynikov, X. D. Zou, S. Hovmöller, K. H. Kuo, *Acta Crystallogr. Sect. B* **2006**, *62*, 16.

[39] H. Takakura, C. P. Gómez, A. Yamamoto, M. D. Boissieu, A. P. Tsai, *Nat. Mater.* **2007**, *6*, 58.

[40] E. Brouns, J. W. Visser, P. M. de Wolff, *Acta Crystallogr.* **1964**, *17*, 614.

[41] W. van Aalst, J. den Holander, W. J. A. M. Peterse, P. M. de Wolff, *Acta Crystallogr. Sect. B* **1976**, *32*, 47.

[42] S. van Smaalen, K. D. Bronsema, J. Mahy, *Acta Crystallogr. Sect. B* **1986**, *42*, 43.

[43] R. G. Jordan, Y. Liu, S. L. Qiu, X. Xu, *Phys. Rev. B* **1993**, *47*, 16521.

[44] W. J. Schutte, J. L. de Boer, *Acta Crystallogr. Sect. B* **1993**, *49*, 398.

[45] A. K. Larsson, L. Stenberg, S. Lidin, *Z. Kristallogr.* **1995**, *210*, 832.

[46] A. V. Skripov, D. S. Sibirtsev, Y. G. Cherepanov, B. A. Aleksashin, *J. Phys. Condens. Matter* **1995**, *7*, 4479.

[47] M. Elding-Pontén, L. Stenberg, A. K. Larsson, S. Lidin, K. Ståhl, *J. Solid State Chem.* **1997**, *129*, 231.

[48] L. A. Bendersky, R. M. Waterstrat, *J. Alloys Compd.* **1997**, *252*, L5.

[49] T. E. Mitchell, A. Misra, *Mater. Sci. Eng. A* **1999**, *261*, 106.

[50] S. Lidin, V. Petricek, L. Stenberg, S. Furuseth, H. Fjellvåg, A. K. Larsson, *Solid State Sci.* **2000**, *2*, 353.

[51] R. Caracas, *J. Appl. Crystallogr.* **2002**, *35*, 120.

[52] O. Schwomma, A. Preisinger, H. Nowotny, A. Wittmann, *Monatsh. Chem.* **1964**, *95*, 1527.

[53] H. W. Knott, M. H. Mueller, L. Heaton, *Acta Crystallogr.* **1967**, *23*, 549.

[54] G. Zwilling, H. Nowotny, *Monatsh. Chem.* **1973**, *104*, 668.

[55] H. Völlenkle, A. Preisinger, H. Nowotny, A. Wittmann, *Z. Kristallogr.* **1967**, *124*, 9.

[56] W. Jeitschko, E. Parthé, *Acta Crystallogr.* **1967**, *22*, 417.

[57] D. Givord, P. Tenaud, J. M. Moreau, *J. Less-Common Met.* **1986**, *123*, 109.

[58] O. Gourdon, Z. Izaola, L. Elcoro, V. Petricek, G. J. Miller, *Philos. Mag.* **2006**, *86*, 419.

[59] M. Onoda, M. Saeki, *Solid State Ionics* **2004**, *172*, 481.

[60] A. Yamamoto, *Acta Crystallogr. Sect. B* **1982**, *38*, 1451.

[61] P. Bak, *Phys. Rev. Lett.* **1985**, *54*, 1517.

[62] R. K. Rastsvetaeva, N. B. Bolotina, A. N. Sapozhnikov, A. A. Kashaev, A. Schoenleber, G. Chapuis, *Kristallografiya* **2002**, *47*, 449.

[63] K. Burkhardt, K. Schubert, R. S. Toth, H. Sato, *Acta Crystallogr. Sect. B* **1968**, *24*, 137.

[64] S. Samson, *Nature* **1962**, *195*, 259.

[65] W. Jung, *J. Less-Common Met.* **1984**, *97*, 253.

[66] A. V. Arakcheeva, O. G. Karpinskii, V. E. Kolesnichenko, *Kristallografiya* **1988**, *33*, 1523.

[67] O. Gourdon, G. J. Miller, *Chem. Mater.* **2006**, *18*, 1848.

[68] R. E. Peierls, *Quantum Theory of Solids*, Oxford University Press, Oxford, **1955**.

[69] J. S. Miller, A. J. Epstein, *Prog. Inorg. Chem.* **1976**, *20*, 1.

[70] J. K. Burdett, *Prog. Solid State Chem.* **1984**, *15*, 173.

[71] O. Schwomma, H. Nowotny, A. Wittmann, *Monatsh. Chem.* **1964**, *95*, 1538.

[72] G. Flieher, H. Völlenkle, H. Nowotny, *Monatsh. Chem.* **1968**, *99*, 877.

[73] O. G. Karpinskii, B. A. Evseev, *Izv. Akad. Nauk SSSR Neorg. Mater.* **1969**, 5, 438.

[74] J. A. Lee, G. V. Raynor, *Proc. Phys. Soc.* **1954**, *B67*, 737.

[75] V. Petricek, M. Dusek, L. Palatinus, Jana2000: The Crystallographic Computing System, Institute of Physics, Praha (Czech Republic), **2000**.

[76] V. Petříček, M. Dušek, *Z. Kristallogr.* **2004**, *219*, 692.

[77] M. McMahon, R. Nelmes, *Z. Kristallogr.* **2004**, *219*, 742.

[78] M. I. McMahon, R. J. Nelmes, U. Schwarz, K. Syassen, *Phys. Rev. B* **2006**, *74*, 140102.

[79] M. I. McMahon, T. Bovornratanaraks, D. R. Allan, S. A. Belmonte, R. J. Nelmes, *Phys. Rev. B* **2000**, *61*, 3135.

[80] R. J. Nelmes, D. R. Allan, M. I. McMahon, S. A. Belmonte, *Phys. Rev. Lett.* **1999**, *83*, 4081.

[81] O. Degtyareva, M. I. McMahon, R. J. Nelmes, *Phys. Rev. B* **2004**, *70*, 184119.

[82] M. I. McMahon, O. Degtyareva, R. J. Nelmes, *Phys. Rev. Lett.* **2000**, *85*, 4896.

[83] U. Häussermann, O. Degtyareva, A. S. Mikhaylushkin, K. Söderberg, S. I. Simak, M. I. McMahon, R. J. Nelmes, R. Norrestam, *Phys. Rev. B* **2004**, *69*, 134203.

[84] L. Cario, P. Palvadeau, A. Lafond, C. Deudon, Y. Moëlo, B. Corraze, A. Meerschaut, *Chem. Mater.* **2003**, *15*, 943.

[85] A. Meerschaut, P. Rabu, J. Rouxel, *J. Solid State Chem.* **1989**, *78*, 35.

[86] S. van Smaalen, *J. Phys. Condens. Matter* **1991**, *3*, 1247.

[87] A. Jobst, S. van Smaalen, *Acta Crystallogr. Sect. B* **2002**, *58*, 179.

[88] W. Müller, K. Volk, *Z. Naturforsch. B* **1978**, *33*, 275.

[89] M. L. Fornasini, M. Pani, *Acta Crystallogr. Sect. C* **1986**, *42*, 394.

[90] M. L. Fornasini, A. Mugnoli, A. Palenzona, *J. Less-Common Met.* **1989**, *154*, 149.

[91] B. H. Chen, B. W. Eichhorn, P. E. Fanwick, *Inorg. Chem.* **1992**, *31*, 1788.

[92] G. Nover, K. Schubert, *J. Less-Common Met.* **1980**, *75*, 51.

[93] J. T. Schmidt, S. Lee, D. C. Fredrickson, M. Conrad, J. Sun, B. Harbrecht, *Chem. Eur. J.* **2007**, *13*, 1394.

[94] M. Evain, M. Queignec, R. Brec, J. Rouxel, *J. Solid State Chem.* **1985**, *56*, 148.

[95] A. Bezinge, K. Yvon, H. F. Braun, J. Muller, H. U. Nissen, *Phys. Rev. B* **1987**, *36*, 1406.

[96] Z. B. Zhao, S. Y. Hong, *J. Phys. Condens. Matter* **1992**, *4*, 9221.

[97] A. Bezinge, H. F. Braun, J. Muller, K. Yvon, *Solid State Commun.* **1985**, *55*, 131.

[98] I. B. Gubich, P. Y. Zavalii, Y. B. Kuzma, *Inorg. Mater.* **1993**, *29*, 301.

[99] P. Y. Zavalii, Y. B. Kuzma, L. V. Zavalii, *Kristallografiya* **1990**, *35*, 638.

[100] Z. B. Zhao, S. K. Xia, C. R. Wang, R. Z. Ma, *J. Phys. Condens. Matter* **1989**, *1*, 7513.

[101] P. Y. Zavalij, S. I. Mykhalenko, Y. B. Kuz'ma, *J. Alloys Compd.* **1994**, *203*, 55.

[102] Y. N. Grin, U. P. Yarmolyuk, V. E. Zavodnik, *Kristallografiya* **1984**, *29*, 228.

[103] O. Gourdon, E. Jeanneau, M. Evain, S. Jobic, R. Brec, H. J. Koo, M. H. Whangbo, *J. Solid State Chem.* **200**1, *162*, 103.

[104] Y. Komura, T. Ohba, K. Kifune, H. Hirayama, T. Tagai, N. Yamada, T. Ohoyama, *Acta Crystallogr. Sect. C* **1987**, *43*, 7.

[105] S. Cirafici, M. L. Fornasini, *J. Less-Common Met.* **1989**, *154*, 79.

[106] W. Wopersnow, K. Schubert, *J. Less-Common Met.* **1976**, *48*, 79.